

Master Thesis

**Viscoelastic modelling of
grounding line migration**

Sebastian Beyer

Institute of Geophysics
University of Hamburg
September 2014

Hiermit erkläre ich, dass ich diese Arbeit selbstständig angefertigt und ausschließlich die angeführten Quellen als Hilfsmittel verwendet habe. Die Arbeit habe ich vorher nicht in einem anderen Prüfungsverfahren eingereicht. Die schriftliche Fassung entspricht der auf dem elektronischen Speichermedium eingereichten. Der Veröffentlichung der Masterarbeit stimme ich zu.

Hamburg, September 2014

Sebastian Beyer

Abstract

In this thesis we investigate the influence of tides to the dynamics of ice sheet – ice shelf systems with numerical modelling. Tides play an important role in these systems by moving ice shelves and modulating the flow velocities of ice streams even far upstream. The grounding line as the boundary between the shelf and the ice sheet plays a crucial role in the mass balance and general stability of an ice sheet. It has been observed to migrate in response to tidal forcing, but the exact mechanisms and consequences are not yet understood in detail.

On short timescales, as present in tidal forcing, we need to account for the viscoelastic character of glacier ice and choose a Maxwell model as an appropriate rheological representation. We develop and implement a viscoelastic full Stokes ice flow model and implement it in the finite element software COMSOL Multiphysics. Two different test setups are used to verify our flow model and show good agreement.

In our model we are able to identify two processes, which control ice flow variations with tides. Uplifting of the ice shelf leads to retreat of the grounding line and therefore less area of the ice base is in contact with the bedrock. This leads to smaller basal shear stress, resulting in an increase in flow velocity. Additionally high tide causes increased normal stress at the ice – water boundary, which slows the ice flow. When forced with the S_2 (12 h) and M_2 (12.42 h) tidal constituents, we observe a non-linear interaction, which leads to a perturbation of the horizontal flow velocity close to the M_{sf} (14.76 d) constituent. By not including tides and viscoelasticity into ice models we commit significant errors for the estimation of the flux across the grounding line and the resulting mass balance. For our experimental setup this error depends on the elastic parameter and we obtain a maximal error of 3.75 %. We also observe a general retreat of the grounding line due to tidal forcing. This implies that tides possibly lead to a different equilibrium of the grounding line position.

Kurzfassung

In dieser Masterarbeit untersuchen wir den Einfluss von Tiden auf die Dynamik von Eisschild – Schelfeis Systemen durch numerische Modellierung. Tiden spielen hierbei eine wichtige Rolle, da sie die Schelfeise auf und ab bewegen und damit die Fließgeschwindigkeit des Eises bis in den Eisschild beeinflussen. Die Aufsatzlinie bildet die entscheidende Grenze zwischen dem Eisschild und dem Schelfeis. Sie ist maßgeblich für die Massenbilanz und die generelle Stabilität des Eiskörpers verantwortlich. Messungen haben gezeigt, dass sich diese Linie durch Gezeiten bewegt. Die exakten Mechanismen und Folgen dessen sind bisher nur unzureichend erforscht.

Auf kurzen Zeitskalen, wie sie bei Gezeiten auftreten, verhält sich Eis viskoelastisch. Dieses Verhalten bilden wir in unserem Fließmodell ab, indem wir ein Maxwell Modell für die Beschreibung der Rheologie verwenden. Wir entwickeln ein viskoelastisches Full Stokes Fließmodell und implementieren es in der Finiten Elemente Software COMSOL Multiphysics. Mittels zwei verschiedener Testsetups verifizieren wir das Modell.

In unserem Modell ermitteln wir zwei Prozesse, die für die Modulation der Eisgeschwindigkeiten durch die Tiden verantwortlich sind. Zunächst sorgt das Anheben des Schelfeises dafür, dass weniger Fläche des Eiskörpers in Kontakt mit dem Felsbett ist. Dies führt zu geringerer basaler Reibung und damit zu erhöhter Fließgeschwindigkeit. Gleichzeitig führt ein höherer Wasserstand auch zu größerer Normalspannung an der Eis – Ozean Grenzfläche, was die Fließgeschwindigkeit verringert. Eine nichtlineare Interaktion der S_2 (12 h) und der M_2 (12.42 h) Partialtiden führt zu einer Perturbation der horizontalen Fließgeschwindigkeit mit einer für die M_{sf} (14.76 d) Partialtide typischen Frequenz. Das Vernachlässigen der viskoelastischen Eigenschaften des Eises und des Effekts der Tiden auf den Eiskörper, führt zu systematischen Fehlern bei der Bestimmung des Flusses über die Aufsatzlinie und damit der Massenbilanz. In unserem experimentellen Setup ermitteln wir für diesen Fehler einen maximalen Wert von 3.75%. Außerdem beobachten wir einen, durch Gezeiten verursachten, generellen Rückzug der Aufsatzlinie. Daraus folgern wir, dass Gezeiten einen signifikanten Einfluss auf die Gleichgewichtsposition der Aufsatzlinie haben.

Contents

1	Introduction	1
2	Theory	5
2.1	Balance Equations	5
2.1.1	Mass Balance	5
2.1.2	Momentum Balance	5
2.2	Constitutive Equations	6
2.2.1	Incompressible Newtonian Fluid	6
2.2.2	Rheological Behaviour of Polycrystalline Ice	6
2.2.3	Glen's Flow Law	7
2.2.4	Viscoelastic Rheology Models	8
2.2.5	Maxwell Model	10
2.3	Boundary Conditions	11
2.3.1	Ice Surface	12
2.3.2	Ice Base	12
2.3.3	Calving Front	13
2.3.4	Ice Divide	14
3	Implementation and Verification	15
3.1	Implementation	15
3.1.1	Geometry and Mesh	18
3.1.2	Ice flow Model	20
3.1.3	Boundary Conditions	22
3.1.4	Solver	25
3.2	Verification	27
3.2.1	ISMIP-HOM Experiment D	27
3.2.2	Stress Build-up in a Viscoelastic Maxwell body	30
4	Experiments and Results	33
4.1	Experiments	33
4.1.1	Experiment 1: No migration $M_2 S_2$ tide	33
4.1.2	Experiment 2: High amplitude, M_m tide	34
4.2	Results	34
4.2.1	Experiment 1	34

4.2.2	Experiment 2	42
4.3	Discussion	45
4.3.1	Experiment 1	45
4.3.2	Experiment 2	47
5	Conclusion and Outlook	49
	Bibliography	53
	List of Figures	55
	List of Tables	56

1 Introduction

Glaciers and ice sheets play an important role in the Earth System. They are a crucial component of our planet's climate, directly influencing the radiation balance and global sea level and therefore have a considerable impact, not only on physical but also on social and eco-systems. The ice sheets of Greenland and Antarctica combined contain enough water rise global sea level by 65.66 m (Vaughan et al., 2013). While they are not expected to melt completely in the near future, they are subjected to rising temperatures and their contribution to sea level rise is increasing. A comparison of elevation change rates between 2011 and 2014 to rates between 2003 and 2009 show that the volume loss has increased by a factor of 3 for West Antarctica and by a factor of 2.5 for Greenland. An estimate of the combined volume change over the observed period can be given as $(-503 \pm 107) \text{ km yr}^{-1}$ (Helm et al., 2014). To the total sea level rise of $(3.2 \pm 0.4) \text{ mm yr}^{-1}$ over the period from 1993 to 2010 the ice sheets of Antarctica and Greenland contribute about 0.6 mm yr^{-1} (Vaughan et al., 2013).

An ice sheet gains mass by surface accumulation of precipitation and loses mass through drainage into the surrounding ice shelves, calving off icebergs and, to a lesser extend, due to melt. The grounding line is the boundary between the ice sheet that rests on rigid ground and the floating ice shelf. The flux across this transition zone mainly controls the mass balance of the ice sheet and is therefore one of the most important quantities to study. It is however difficult to determine the position of the grounding line (and as a consequence also the flux), since there is no obvious indicator at the surface.

Ice shelves are formed by the ice draining from ice streams and outlet glaciers and surround most of the Antarctic coast. They play a crucial role for the stability of the ice sheets due to their buttressing effect which is caused by lateral shear margins in bay areas and reduces the flow velocity of the ice. Over the last decades ice shelves along the Antarctic Peninsula have become unstable, resulting in increasing flow velocities of outlet glaciers. Recent studies rise the concern, that the marine portion of the West Antarctic Ice Sheet (WAIS) may have started an irreversible collapse (Rignot et al., 2014; Joughin et al., 2014).

It is crucial to undertake further research on the principles that drive ice sheet – ice shelf interaction and to develop reliable numerical ice models, to predict the future response of large ice sheets and their contribution to sea level and climate change.

While ice sheets rest on rigid ground, ice shelves float on the ocean and therefore are affected by tides. The vertical movement of the ice shelf leads to elastic bending around the grounding line. Hence the grounding line migrates in response to the tide as sketched in Fig. 1.1. The area in which the bending occurs is called hinge zone. It can be observed

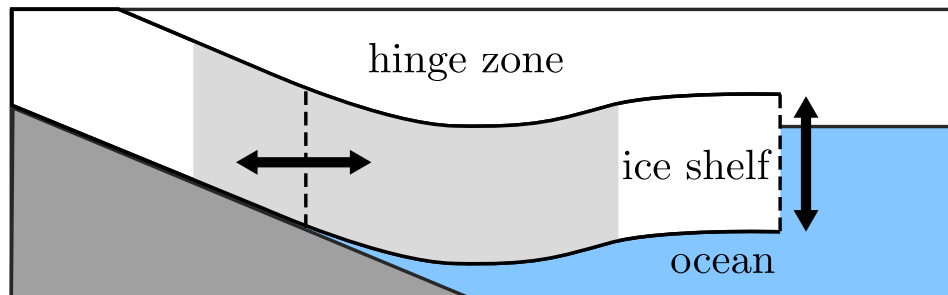


Figure 1.1: Principle of the grounding line – ocean tide interaction. Variations in sea level displace the ice shelf and since the ice stream is fixed, bending occurs in the transition zone between ice shelf and ice sheet (hinge zone). The grounding line migrates back and forth with the tides.

in interferometric Synthetic Aperture Radar (InSAR) satellite images, where the phase shift in the signal is used to measure very small displacements. In Fig. 1.2 such an image from an area of the Wilkins shelf is presented. Areas where the ice body is bending are covered by color circles, called *fringe belts*. From this it is possible to locate the position of the grounding line and also the amplitudes of the tides can be determined. Depending on the topography and amplitude of the tides, the hinge zone can be several kilometers wide and marks the area where the grounding line migrates. While this enables us to observe

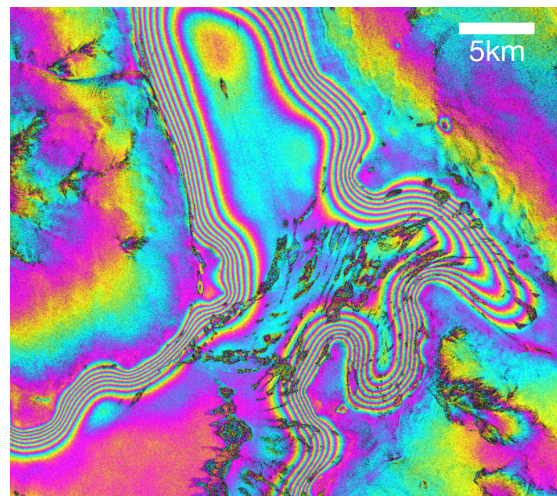


Figure 1.2: Quadruple InSAR image of the Wilkins shelf ice. Areas of horizontally varying vertical displacements (flexure) are visible as color cycles. The fringe belt marks the area of bending. It consists of seven fringes which corresponds to a vertical displacement of about 20 cm for the shelf (Moll, 2007).

the position of the grounding line on timescales of months (depending on the repeat cycle of the satellite), its temporal resolution is not sufficient to help us understanding the

underlying physical processes in detail. This is where numerical models become valuable.

Tidal motion also influences the horizontal velocities of ice shelves and the outlet glaciers and ice streams even far upstream. Velocity variations of up to 20% have been observed and can be attributed to the fact that an uplifted ice shelf has less area in contact with the ground. Hence the basal drag is reduced and this leads to higher velocities (Gudmundsson, 2011; Lohse, 2012).

Ice is a viscoelastic fluid with a non Newtonian rheology. On timescales of months, years and millennia, as usually studied in the realm of climate science, it can be described as a purely viscous fluid. However when looking at tides, which change the load situation of ice shelves on an hourly time scale, the elastic effects have to be considered as well. Therefore an appropriate material model has to be chosen. It needs to be able to correctly incorporate viscous flow on long time scales as well as short term elastic behaviour.

The goal of this thesis is to develop a viscoelastic full Stokes ice model to investigate the role of tides in the dynamics of ice sheet – ice stream interaction. The implementation is done with the Finite Element method in the commercial software COMSOL Multiphysics. Before the flow model can be used to make any predictions, it has to be tested and verified against analytical solutions and other models. We use an idealized two dimensional ice sheet – ice shelf geometry to perform different experiments. The main focus lies on understanding the processes involved in the modulation of the flow velocity by tidal forcing and to identify the influence of specific variables, such as tidal periods, elastic parameters and bedrock inclination.

This thesis is structured as follows: The second chapter (Chapter 2) introduces the underlying theory of the ice model. Balance equations for mass and momentum and the resulting full Stokes system of equations are presented. The rheological behaviour of ice is discussed and the equations for the Maxwell model are derived. Chapter 3 describes the numerical implementation in the Finite Element software COMSOL and verifies the correct operation of the model at two test cases. The detailed description of experiments and results is the subject of Chapter 4 and in Chapter 5 the conclusions are summarized and an outlook for further research is given.

2 Theory

In this chapter we outline the theoretical foundations of the flow model used. The viscous flow of large ice masses can be described using continuum mechanics. In the model glacier ice is defined as an incompressible, isothermal, nonlinear viscoelastic fluid. The governing equations are balance equations for mass and momentum. They are completed by constitutive material equations suitable to account for long term nonlinear viscous creep as well as short term elastic responses. Though ice is considered incompressible, the equations are introduced in their general compressible form and subsequently adapted for incompressibility. Continuum mechanics is a wide field and better described in depth elsewhere. Thus the following derivation originates mostly from Greve and Blatter (2009) and only the most important equations are presented in two dimensional form. We can not introduce the concept of Finite Elements methods in this work, but we give a brief overview about the equations and procedures invoked in solving of the equations in Section 3.1.4.

2.1 Balance Equations

2.1.1 Mass Balance

In general, the mass balance of an incompressible continuum can be written as

$$\operatorname{div} \boldsymbol{v} = 0. \quad (2.1)$$

This equation is also called the *continuity equation*, and represents a divergence-free (solenoidal) velocity field.

2.1.2 Momentum Balance

The momentum balance arises from *Newton's second law of motion* and requires the change of momentum over time to be in equilibrium with the forces applied to the body. These forces are volume forces \boldsymbol{f} (i.e. gravity, coriolis force) and surface forces $\boldsymbol{\sigma}$ (such as water pressure or shear stresses). Due to very slow flow and high viscosity of glacier ice, inertial forces can be neglected (Greve and Blatter, 2009, pp. 62-64) and only gravitational attraction remains as a volume force. The resulting equation reads as

$$\operatorname{div} \boldsymbol{\sigma} + \boldsymbol{f} = 0, \quad (2.2)$$

with the *Cauchy stress tensor* $\boldsymbol{\sigma}$, which represents the relevant surface forces. This tensor is symmetric (due to *balance of angular momentum* (Greve and Blatter, 2009, pp. 33-34))

and is commonly split into a deviatoric or viscous part σ^D and a pressure dependent hydrostatic part $p\mathbf{I}$

$$\boldsymbol{\sigma} = \boldsymbol{\sigma}^D - p\mathbf{I}, \quad (2.3)$$

where $p = -1/3 \operatorname{tr} \boldsymbol{\sigma}$ denotes the pressure and \mathbf{I} the identity tensor. As volume force \mathbf{f} we only consider the gravity force $\rho\mathbf{g}$, where \mathbf{g} has the form $\mathbf{g} = (0, -g)^\top$. This leads to the *Stokes equation*

$$\operatorname{div}(\boldsymbol{\sigma}^D - p\mathbf{I}) = -\rho\mathbf{g}. \quad (2.4)$$

2.2 Constitutive Equations

In the previous section we derived balance equations of mass and momentum. Knowing the force \mathbf{f} leads to a set of 3 equations (mass balance: 1, momentum balance: 2) for 6 unknowns (p : 1(scalar), \mathbf{v} :2 (2D vector), $\boldsymbol{\tau}$:3 (symmetric 2×2 tensor)). The system is therefore underdetermined and requires additional *closure*-relations between the quantities (stresses and strains in our case). The system of equations is universally true for every possible material, since we do not make any assumptions on the material behaviour. The description of material properties is incorporated into the model using constitutive relations to complement the balance equations.

2.2.1 Incompressible Newtonian Fluid

Although ice is of highly nonlinear nature, it is helpful to consider first the simpler case of a *Newtonian fluid*. A incompressible Newtonian fluid is a fluid in which the deviatoric viscous stresses $\boldsymbol{\sigma}^D$ are linearly proportional to the strain rate tensor $\dot{\boldsymbol{\epsilon}}$:

$$\boldsymbol{\sigma}^D = 2\eta\dot{\boldsymbol{\epsilon}}, \quad (2.5)$$

where the viscosity η is constant (J. Altenbach and H. Altenbach, 1994, p. 234). Note that $\dot{\boldsymbol{\epsilon}}^D = \dot{\boldsymbol{\epsilon}}$, due to the mass balance Eq. (2.1) being equivalent to $\operatorname{tr} \dot{\boldsymbol{\epsilon}} = 0$. The linearized strain rate tensor $\dot{\boldsymbol{\epsilon}}$ is a symmetric second order tensor with the components

$$\dot{\epsilon}_{ij} = \frac{1}{2} \left(\frac{\partial v_i}{\partial x_j} + \frac{\partial v_j}{\partial x_i} \right). \quad (2.6)$$

2.2.2 Rheological Behaviour of Polycrystalline Ice

Glacier ice appears in nature usually as a cluster of microscopic ice crystals, called *crystallites* or *grains*, which constitute a *polycrystalline* body. We can assume that the orientation of single crystals in this compound is random and therefore the macroscopic behaviour is isotropic.

If a constant shear stress τ is applied to a block of polycrystalline ice, the shear angle γ is measureable over time. The qualitative result is shown in Fig. 2.1b. The curve shows an instantaneous elastic deformation, followed by decreasing of the shear rate $\dot{\gamma}$ due to the raise of geometric incompatibilities of the crystallites. This phase is called *primary*

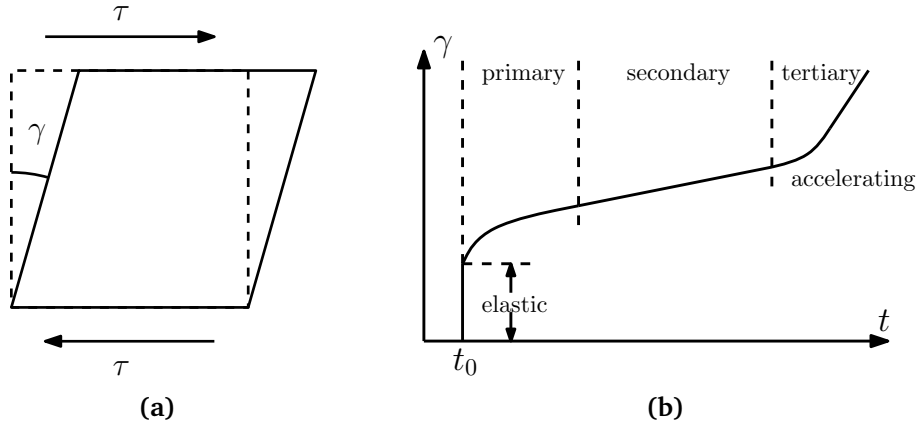


Figure 2.1: (a) Shear experiment for a block of polycrystalline ice. The constant shear stress is denoted by τ .
 (b) Observed shear angle γ over time t . Reproduced from Greve and Blatter (2009).

creep. It is followed by *secondary creep*, where the shear rate is minimal and the shear angle increases linearly in time accordingly. In case of high temperatures and/or stresses, it is also possible to observe a phase of *tertiary creep* for large time scales, consisting of a short acceleration and then a considerably higher constant shear rate as in the second phase. This can be attributed to *dynamic recrystallization* of grains.

2.2.3 Glen's Flow Law

Laboratory experiments (e.g. Glen, 1955) suggest a power law as relation between the deviatoric stress tensor σ^D and the strain rate tensor $\dot{\epsilon}$. In the generalized form of Nye (1957) it can be written as

$$\dot{\epsilon}_{ij} = EA\sigma_e^{Dn-1}\sigma_{ij}^D, \quad (2.7)$$

with σ_e^D being the effective deviatoric stress, the second invariant of the deviatoric stress tensor. This equation is called *Glen's flow law*. The *flow-rate factor* A is usually dependent on temperature and water content, but is assumed constant in this study. The *enhancement factor* E parameterizes otherwise unaccounted physical contributions, such as impurities or fractures in the ice and is taken to be 1 in this study. The exponent n is set to a common value of 3 (Paterson, 1994).

It is possible to write Glen's flow law in its inverse form

$$\sigma^D = 2\eta\dot{\epsilon} \quad \text{with} \quad \eta(\dot{\epsilon}_e) = \frac{1}{2}(EA)^{-1/n}\dot{\epsilon}_e^{(1-n)/n}. \quad (2.8)$$

In contrast to the Newtonian fluid, the relation between stress and strain rates is nonlinear. The viscosity $\eta(\dot{\epsilon}_e)$ depends on the effective strain rate $\dot{\epsilon}_e$

$$\dot{\epsilon}_e = \sqrt{\frac{1}{2} \text{tr} \dot{\epsilon}^2}. \quad (2.9)$$

In case of incompressibility (Eq. (2.1)) and two dimensions in x,z direction Eq. (2.9) simplifies to

$$\dot{\epsilon}_e = \sqrt{\left(\frac{\partial v_x}{\partial x}\right)^2 + \frac{1}{4}\left(\frac{\partial v_x}{\partial z} + \frac{\partial v_z}{\partial x}\right)}. \quad (2.10)$$

For numerical stability it is necessary to add a small value of 10^{-30} to $\dot{\epsilon}_e$ to keep the term non-zero.

Glen's flow law is able to describe the behaviour of ice in the secondary creep phase very well. It can, however, not account for elastic deformation on short timescales, which we assess in this study. Therefore, a rheological model which incorporates this behaviour, needs to be developed.

2.2.4 Viscoelastic Rheology Models

Unless otherwise stated, the following deductions on viscoelasticity are compiled from Malvern (1969). For the development of more sophisticated models, it is convenient to use so called *spring-dashpot* models. These one dimensional mechanical analog models use *Hookean* springs to represent the instantaneous elastic deformation (i.e. the stress is linearly dependent on strain) of the material and Newtonian dashpots to denote creep behaviour (i.e. stress depends on the rate of strain), shown in Fig. 2.2. Axial force in the

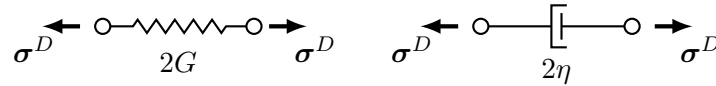


Figure 2.2: Hookean spring (left) and Newtonian dashpot (right).

model defines stress in the continuum, while axial elongation and velocity correspond to strain and strain rate. If we assume small deformation and only consider uniform strain with no rotation, then the velocity can be identified with the rate of strain (This could be generalized for large deformations using e.g. convected derivatives to obtain *frame indifference* as described in Christensen (1982, pp. 340-341), but is not necessary and therefore not done in our application).

Stresses and strains can be decomposed into volumetric components, changing the volume, and deviatoric components, which change the shape of the body. (see Section 2.1.2). Hence the stress in Fig. 2.2 is denoted by σ^D and the stresses in the spring and damper are $\sigma^D = 2G\epsilon^D$ and $\sigma^D = 2\eta\dot{\epsilon}^D$ respectively. Herein G is the shear modulus which defines the rigidity of the spring in the case of pure shear or shear stress and η is the viscosity. These relations are valid for a constant cause (stress or strain). Time dependent causes ($\sigma(t)$, $\epsilon(t)$) can be treated as a series of constant causes applied at different times. Their respective responses are independent of each other and add up cumulatively to the time dependent response. This principle is called *Boltzmann Superposition Principle*.

A dashpot and a spring connected in parallel are called a *Kelvin-Voigt* unit, while in series they represent a *Maxwell* unit. Both units show viscoelastic properties, but on

long timescales the Kelvin-Voigt unit behaves like a solid and the Maxwell unit as a fluid. Over tidal timescales ice acts as a viscoelastic medium and its rheological behaviour, observed in experiments, can be modelled using a four-element Burger model as shown in Fig. 2.3a (e.g. Jellinek and Brill, 1956; Reeh et al., 2003). Despite being a relative simple model, it is able to exhibit instantaneous elastic deformation, primary creep and secondary creep. The instantaneous elastic behaviour is governed by the spring in the Maxwell unit, while the Kelvin unit accounts for primary creep. On long timescales only the damper of the Maxwell unit remains significant in driving the steady-state viscous deformation.

In his study of ice-stream response to tides and the basal sliding law Gudmundsson (2011) found that with appropriate parameters, a Maxwell model can be used to reproduce the rheological behaviour of the Burger model on the timescales of interest. Only for loading periods of less than 100 s the models have significant differences. In Fig. 2.3 the Maxwell model and the strain response to sudden stress is compared to the Burger model.

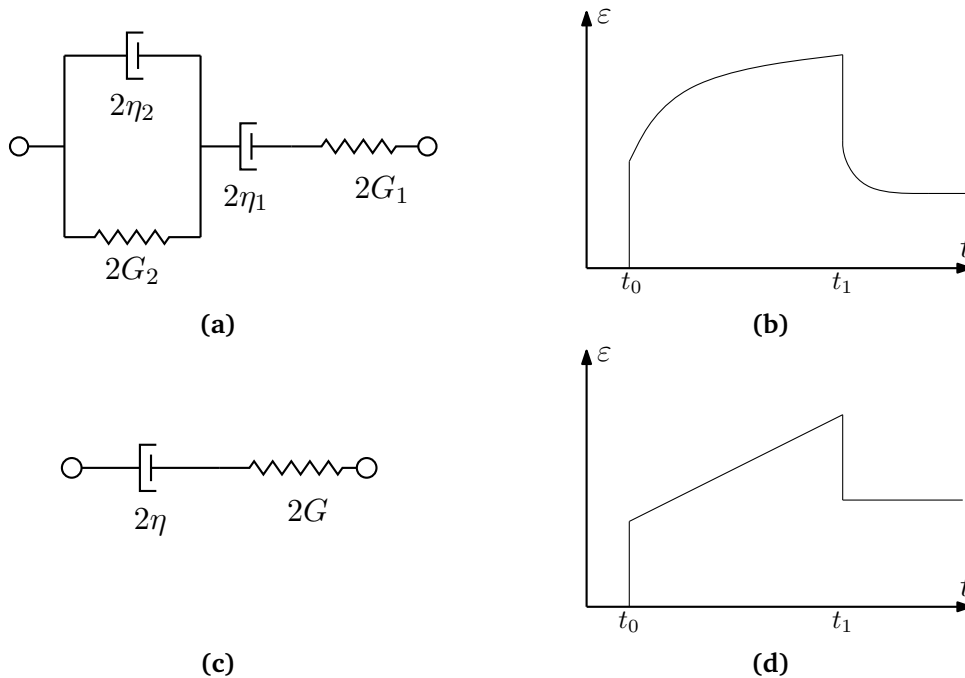


Figure 2.3: Comparison of the Burger model used by Jellinek and Brill (1956) to the Maxwell model used by Gudmundsson (2011) and this study.

- (a) The Burger model consists of a Kelvin unit and a Maxwell unit in series.
- (b) Resulting displacement ε of the Burger model in response to a sudden stress at $t = t_0$, which is released at $t = t_1$.
- (c) The Maxwell model consists of a Newtonian damper and a hookean spring.
- (d) Resulting displacement ε of the Maxwell model to the same stress.

By using a Maxwell model instead of a Burger model the amount of unknown material parameters is reduced and also the complexity and therefore computational time is significantly smaller.

2.2.5 Maxwell Model

To obtain an equation for the Maxwell model, we use that in serial connection the total stress is equal to the stress in every single element

$$\boldsymbol{\sigma}^D = \boldsymbol{\sigma}_E^D = \boldsymbol{\sigma}_V^D \quad (2.11)$$

and the total displacement is the sum of the displacements of all elements

$$\boldsymbol{\varepsilon}^D = \boldsymbol{\varepsilon}_E^D + \boldsymbol{\varepsilon}_V^D, \quad (2.12)$$

where the subscripts $_E$ and $_V$ denote the elastic and viscous components respectively. Stresses in the elements can be written as

$$\boldsymbol{\sigma}_E^D = 2G\boldsymbol{\varepsilon}_E^D \quad (\text{Hookean spring}) \quad (2.13)$$

$$\boldsymbol{\sigma}_V^D = 2\eta\dot{\boldsymbol{\varepsilon}}_V^D. \quad (\text{Newtonian dashpot}) \quad (2.14)$$

Starting from the displacement Eq. (2.12) we take the derivative over time and insert the specific displacements from Eq. (2.13) and Eq. (2.14) to obtain

$$\dot{\boldsymbol{\varepsilon}}^D = \frac{1}{2G}\dot{\boldsymbol{\sigma}}_E^D + \frac{1}{2\eta}\boldsymbol{\sigma}_V^D. \quad (2.15)$$

Due to the stresses being equal in all elements, we can write

$$\dot{\boldsymbol{\varepsilon}}^D = \frac{1}{2G}\dot{\boldsymbol{\sigma}}^D + \frac{1}{2\eta}\boldsymbol{\sigma}^D, \quad (2.16)$$

which is the commonly known form for the deviators of the Maxwell model. It is also possible to express Eq. (2.16) in terms of elastic deformation $\boldsymbol{\varepsilon}_E$ by inserting Eq. (2.13) and multiplying by η :

$$\eta\dot{\boldsymbol{\varepsilon}}^D = \eta\dot{\boldsymbol{\varepsilon}}_E^D + G\boldsymbol{\varepsilon}_E^D. \quad (2.17)$$

For the volumetric component we assume ice to be purely elastic under hydrostatic pressure:

$$\text{tr } \boldsymbol{\sigma} = 3K \text{tr } \boldsymbol{\varepsilon}, \quad (2.18)$$

where K is the bulk modulus of the Maxwell model and we obtain the equation for the total stress:

$$\boldsymbol{\sigma} = K \text{tr } \boldsymbol{\varepsilon} + \boldsymbol{\sigma}^D. \quad (2.19)$$

Under the assumption of incompressibility (see Section 2.2.1) the total stress $\boldsymbol{\sigma}$ and the total strain $\boldsymbol{\varepsilon}$ are equal to their deviatoric counterparts $\boldsymbol{\sigma}^D$ and $\boldsymbol{\varepsilon}^D$ and Eq. (2.17) simplifies to

$$\eta\dot{\boldsymbol{\varepsilon}} = \eta\dot{\boldsymbol{\varepsilon}}_E + G\boldsymbol{\varepsilon}_E, \quad (2.20)$$

which we use in the implementation.

For an isotropic material there are only two independent constants, therefore the shear modulus G and the bulk modulus K are expressible with the Young's modulus E and the Poisson's ratio ν :

$$G = \frac{E}{2(1 + \nu)}, \quad K = \frac{E}{3(1 - 2\nu)}. \quad (2.21)$$

For glacier ice we follow Gudmundsson (2011) and assume values of E between 1 GPa and 140 GPa. We set $\nu = 0.5$ as we consider ice to be incompressible.

2.3 Boundary Conditions

The balance equations previously derived are only valid under the assumption of continuously differentiable fields which lie completely inside the observed volume. This assumption does not hold at the interfaces with the surroundings and the equations are not longer valid. Therefore, additional *jump conditions* or boundary conditions have to be formulated. Consequently a kinematic condition, specifying the movement of the interface in relation to the fluid flow, and a dynamic condition, taking into account the force balance at the surface, have to be prescribed. We will give the relevant conclusions, transformed into two dimensional form, and refer to Greve and Blatter (2009) for the complete deduction again.

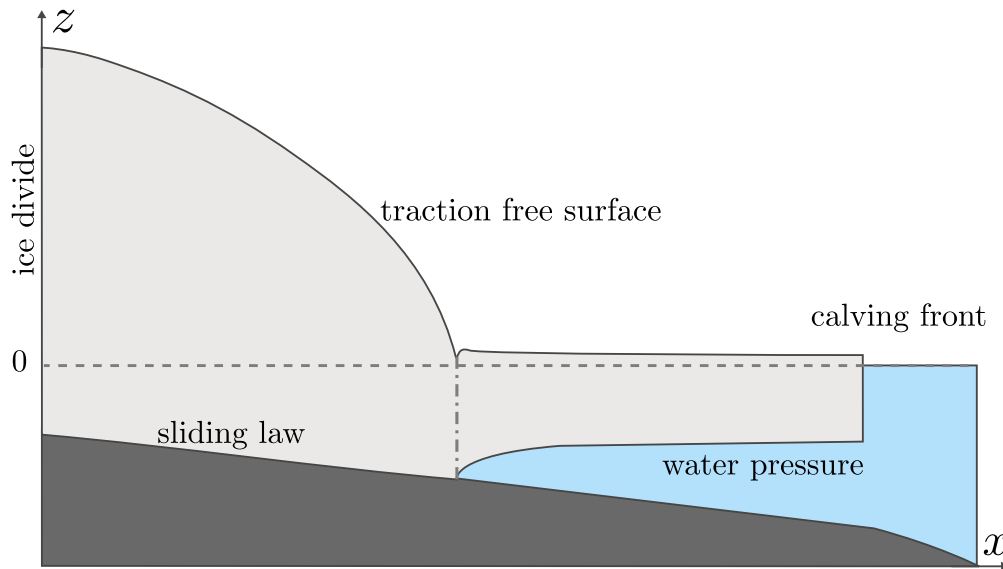


Figure 2.4: Geometry of the ice sheet - ice shelf system with indicated boundary conditions.

2.3.1 Ice Surface

The ice surface describes the stress-free interface between the ice body and the atmosphere and can be given in its implicit form

$$F_s(x, z, t) = z - z_s = 0, \quad (2.22)$$

where z_s is the position of the upper surface. Its kinematic evolution reads:

$$\frac{\partial z_s}{\partial t} + v_x \frac{\partial z_s}{\partial x} - v_z = N_s a_s^\perp = a_s, \quad (2.23)$$

where N_s is short for the gradient norm,

$$N_s = |\text{grad } F_s| = \left(1 + \left(\frac{\partial z_s}{\partial x} \right)^2 \right)^{1/2}, \quad (2.24)$$

and a_s^\perp is the *accumulation-ablation function* or *surface mass balance*. A positive value of a_s^\perp signifies accumulation and a negative value ablation.

For the dynamic condition we assume a stress-free surface. Stress-free means that atmospheric pressure and wind stress can be neglected and therefore implies

$$\mathbf{n} \cdot (\boldsymbol{\sigma} \cdot \mathbf{n}) = 0 \quad (2.25)$$

$$\mathbf{t} \cdot (\boldsymbol{\sigma} \cdot \mathbf{n}) = 0 \quad (2.26)$$

at the surface, where \mathbf{n} is the unit normal vector of the surface pointing outward and \mathbf{t} the tangential vector to the surface ($\mathbf{n} = \text{grad } F_s / |\text{grad } F_s|$).

2.3.2 Ice Base

In a similar fashion the kinematic equation at the ice base can be derived

$$\frac{\partial z_b}{\partial t} + v_x \frac{\partial z_b}{\partial x} - v_z = 0, \quad (2.27)$$

neglecting accretion of sea water by refreezing or melt of bottom ice.

For the dynamic condition we need to distinguish between areas that are in contact with the bedrock and areas where the ice is floating freely on ocean water. The position of the grounding line x_{grl} , and therefore the location of the floating and grounded parts, is not known in advance and therefore part of the solution. This can be treated as a contact problem as described in Durand et al. (2009). We consider the ice to be in contact with the bedrock at a point x if the distance in between equals zero and additionally the stress applied from the ice to the bedrock is larger than the sea-water pressure. On the contrary the ice is considered to float if the ice base z_b is above the bedrock or if it touches the bedrock and the sea-water pressure p_w is larger than the normal stress $\sigma_{nn} = \mathbf{n} \cdot (\boldsymbol{\sigma} \cdot \mathbf{n})$ exerted by the ice. Hence the ice-bedrock boundary condition has to be applied if

$$z_b(x, t) = b(x) \quad \text{and} \quad -\sigma_{nn}|_b > p_w(z_b, t), \quad (2.28)$$

and the ice-sea boundary condition applies if

$$\begin{aligned} & z_b(x, t) > b(x), \\ \text{or } & z_b(x, t) = b(x) \quad \text{and} \quad -\sigma_{nn}|_b \leq p_w(z_b, t), \end{aligned} \quad (2.29)$$

where $b(x)$ is the position of the bedrock and $|_b$ indicates, that the value is to be taken at the bottom surface. In the implementation we approximate σ_{nn} as $\rho g H$, because the pressure has a singularity at the grounding line.

For the ice-bedrock boundary the ice is not allowed to penetrate into the bed and a non-linear friction law (*Weertman-type*) is applied:

$$\begin{aligned} & \mathbf{v} \cdot \mathbf{n} = 0, \\ & \underbrace{\mathbf{t} \cdot (\boldsymbol{\sigma} \cdot \mathbf{n})|_b}_{\tau_b} = -\beta^2 \underbrace{\mathbf{t} \cdot \mathbf{u}}_{v_b}. \end{aligned} \quad (2.30)$$

The basal shear stress or basal drag τ_b is related to the sliding velocity v_b via the basal sliding parameter β^2 , which can be parameterized as

$$\beta^2 = -C|v_b|^{m-1}, \quad (2.31)$$

where C is the basal sliding coefficient (also basal roughness) and the stress exponent m . Therefore Eq. (2.30) can also be written as

$$\begin{aligned} & \mathbf{v} \cdot \mathbf{n} = 0, \\ & \tau_b = C|v_b|^{m-1}v_b. \end{aligned} \quad (2.32)$$

When the ice is floating freely over the ocean the ice-sea boundary equation applies and the shear stress is zero, while the normal stress is equal to the sea-water pressure:

$$\mathbf{t} \cdot (\boldsymbol{\sigma} \cdot \mathbf{n}) = 0 \quad (2.33)$$

$$\mathbf{n} \cdot (\boldsymbol{\sigma} \cdot \mathbf{n}) = -\rho_{sw}\mathbf{g}(z_{sl}(t) - z_b) \cdot \mathbf{n} \quad (2.34)$$

Note that z_b is always negative and therefore, high tide leads to increased normal pressure.

2.3.3 Calving Front

The *calving front* is the point where icebergs are calving off. In this study its position does not change over time, therefore the kinematic equation is omitted. It undergoes the sea-ice pressure $p_w(z, t)$, therefore the dynamic boundary condition reads

$$(\boldsymbol{\sigma} \cdot \mathbf{n}) \cdot \mathbf{n} = p_w(z, t), \quad (2.35)$$

where $p_w(z, t)$ is given by

$$\begin{cases} p_w(z, t) = \rho_{sw}\mathbf{g}(z_{sl}(t) - z), & z < z_{sl}(t) \\ p_w(z, t) = 0, & z \geq z_{sl}(t). \end{cases} \quad (2.36)$$

2.3.4 Ice Divide

Locations that separate opposing flow directions of the ice are called *ice divides*. At these locations there is no surface slope and therefore no driving stress. Stress and flow on one side of the ice divide oppose that on the other side, making the problem axisymmetric. The dynamic boundary condition is given by

$$(\boldsymbol{\sigma} \cdot \boldsymbol{n}) \cdot \boldsymbol{t}_x = 0, \quad (2.37)$$

where \boldsymbol{t}_x is the unit tangent vector in horizontal direction, meaning that there are no tangential stresses at the ice divide.

3 Implementation and Verification

In this chapter we introduce the full-Stokes viscoelastic model. We describe the implementation in the finite element software COMSOL Multiphysics[©] in Section 3.1. The verification of the viscoelastic flow model is presented in Section 3.2. Note that the implementation of the purely viscous grounding line migration had already been done by Martin Rückamp¹, but here the complete process is shown together with the additions necessary for the viscoelastic material model.

3.1 Implementation

For the implementation of the full-Stokes viscoelastic flow model we use COMSOL Multiphysics[©] (Version 4.3b), a commercial finite element software. The *finite element method* is a numerical technique for finding approximate solutions to differential equations, which we will not explain here in detail, but refer to the literature (e.g. Reddy and Gartling, 2010). The COMSOL Software can be used via a graphical user interface (a screenshot is shown in Fig. 3.1), which enables the user to make use of the finite element method and build complex models, without needing to implement the method from scratch. On the other hand it is often a disadvantage not to be able to have a look at and modify the source code. For the development of new models the GUI is very convenient, but for the actual computing process the batch mode, where it is possible to run studies from the commandline, is preferred.

The COMSOL GUI is mainly divided into three parts: *Model Builder*, *Node Properties* and *Graphics*. The model is assembled via the *Model Tree* inside the Model Builder. Different branches, representing components of the model, can be added and configured in *Nodes*. From this COMSOL internally compiles a set of equations, which constitute the model. The branches available by default are *Global Definitions*, *Model*, *Study* and *Results*. In *Global Definitions* parameters that can be accessed everywhere in the model can be defined. We use that for physical constants as listed in Table 3.1. The Model node is subdivided into several subnodes and contains the actual model. It consists of (*Local Definitions*, *Geometry*, *Material* (which we do not use), various *Physics* and *Mesh*). We use the local definitions to enter dependent variables for the particular physics. In Table 3.2 all the variables in use are listed, while the explanation follows in the description of the flow model (Section 3.1.2).

¹Alfred Wegener Institute, Helmholtz Centre for Polar and Marine Research, guest scientist at the Institute of Geophysics, University of Hamburg

Table 3.1: Parameters in the viscoelastic ice flow model

name	expression	unit	description
rho_ice	900	kg m ⁻³	ice density
rho_sea	1000	kg m ⁻³	seawater density
g	9.8	m s ⁻²	acceleration of gravity
E	1		enhancement factor
n	3		exponent in Glen's law
A	0.9×10^{-25}	Pa ⁻³ s ⁻¹	rate factor
m	1/3		sliding exponent
C_const	1×10^7	Pa m ^{-1/3} s ^{-1/3}	sliding parameter C
smb	0.5	m yr ⁻¹	surface mass balance a_s
Ee	1.4×10^{10}	N m ⁻²	Young's modulus
nue	0.5		Poisson's ratio
mw	1		Maxwell switch
spy	31 556 926		seconds per year

In the following sections we describe how we implement the geometry and computational mesh in general (Section 3.1.1), the viscoelastic flow model with boundary conditions (Section 3.1.2) and the procedure to solve the resulting model equations (Section 3.1.4).

3.1.1 Geometry and Mesh

The first step in building the model in COMSOL is to create the geometry. COMSOL provides the possibility to create the geometry from basic geometric shapes, such as rectangles and circles and to compose complex outlines with intersection, union and difference operators. The alternative is to describe the geometry via equations and coordinates. By dividing the entire *Model Domain* into smaller *Model Subdomains* specific physics can be applied to part of the model and also be used to control the mesh in particular areas.

Since we use different geometries in the experiments, we describe the general shape here, while the exact setup will be explained in the corresponding experiments. For the ice sheet - ice shelf system we use *Import* in the geometry branch to import an existing geometry. This geometry is the result of a spinup experiment with parameters similar to the *Marine ice sheet model intercomparison project* (MISMIP; Pattyn et al., 2012) experiments (also shown in Table 3.1). The ice rests on a solid bedrock which is described by $b = -s * m - 100\text{m}$ with b measured downwards from $z = 0\text{m}$ and s denoting the slope of the bed. The x coordinate is measured from the leftmost part of the model and the whole model has a length of 800 km. The generation of the initial steady state geometry (spinup) is not part of this thesis and the geometry is kindly provided by Martin Rückamp. In Fig. 3.2 the geometry view of COMSOL is shown. Note that COMSOL does

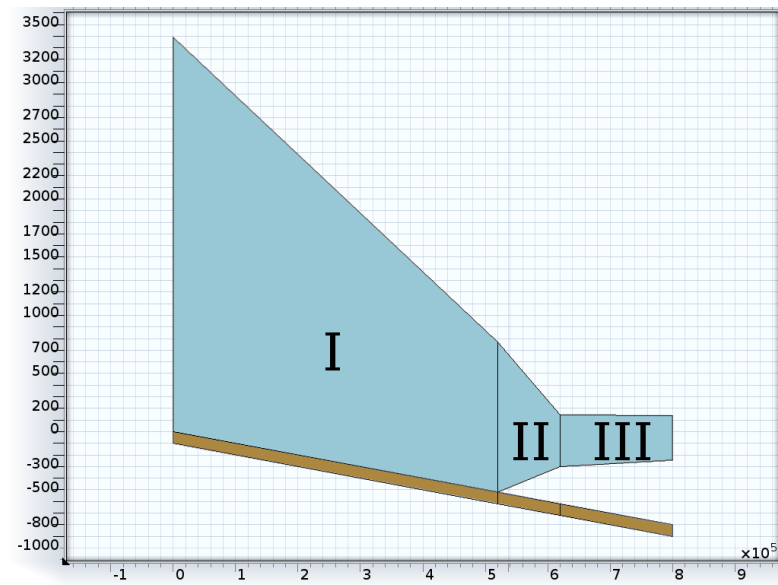


Figure 3.2: Geometry partitioned into domains. The leftmost part (domain I) of the ice is always in contact with the bedrock, the middle part (domain II) is the area in which the grounding line is able to move and the right part (domain III) is always floating.

not show the real geometry until the meshing is done, but the different domains can be seen. There are three upper domains which resemble the ice and three lower domains which contain the bedrock. This partitioning serves the purpose of controlling the mesh

and refine it around the grounding line. We expect that the grounding line does only move in domain II and therefore use a higher mesh resolution in this area.

The mesh of the ice shelf – ice sheet system is a structured grid consisting of quadrilateral elements and is shown in Fig. 3.3. It consists of 5 equidistant vertical layers, which is sufficient for isothermal models of this scale (thermal models generally need more layers towards the bottom). Horizontal resolution is much more important and Durand et al. (2009) have shown that a grid spacing of less than 30 m is necessary to obtain consistent results for a migrating grounding line. We refine our mesh locally in an area around the grounding line to have sufficiently small grid spacing while maintaining reasonable computational costs. A constant grid spacing of H_{\min} is applied to domain II. In domain I and III the grid spacing ranges from H_{\min} , at the edge close to domain II, to $H_{\max,I}$ at the ice divide and $H_{\max,III}$ at the calving front, where the spacing grows in 10% increments relative to their neighbors. Values for H_{\min} and H_{\max} are specified for each experiment.

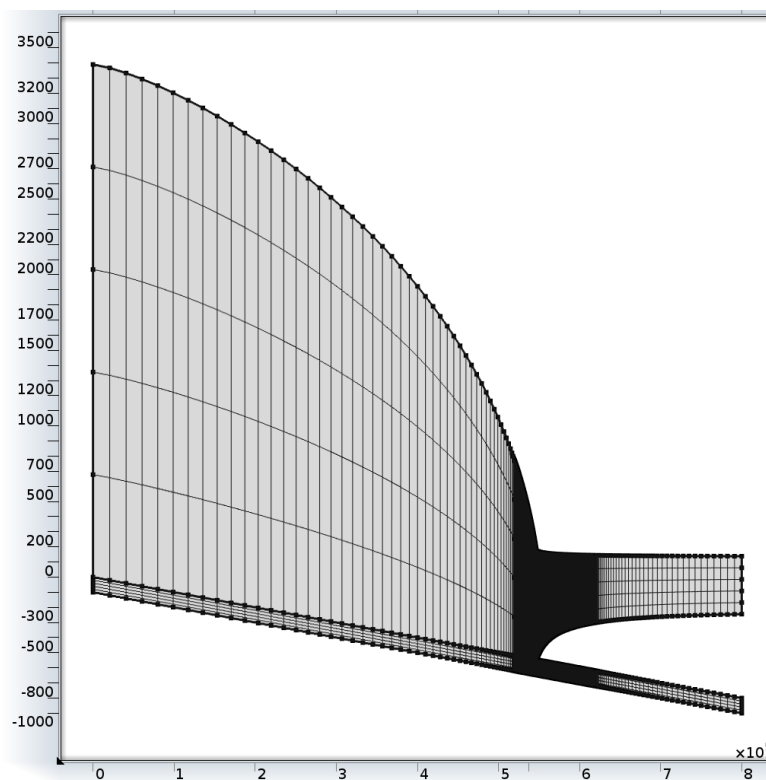


Figure 3.3: Mesh of the flow model with a much higher resolution around the grounding line.

3.1.2 Ice flow Model

For the implementation of the Stokes flow we use the prebuilt *Laminar Flow* physics which we modify to include the Maxwell rheology. The Maxwell PDE (Eq. (2.20)) is implemented as a *Coefficient Form PDE*.

Laminar Flow

The dependent variables in COMSOL notation are u, v, p (v_x, v_z, p). Additional variables needed are set in *Local Definitions* and their values are given in Table 3.2. Since we model ice as an incompressible fluid, we choose that option in the Laminar Flow node. Usually, linear elements (P1) are used to discretize the pressure, while quadratic elements (P2) are used for the velocity. This originates from the Babuška-Brezzi condition, which states that the basis functions for the velocity have to be of higher order than the basis functions for the pressure. Basis functions of the same order can only be used in combination with a numerical stabilization technique, such as COMSOL's streamline diffusion (Galerkin Least Square), as described by Franca and Frey (1992). To reduce computational cost we use (P1) elements for velocity and pressure and activate *Streamline diffusion*. For the *Density* we enter `rho_ice`. We need to add a *Volume Force* node to implement gravity and enter $\mathbf{F} = (0, -\text{rho_ice} * g)$. For purely viscous fluids Glen's flow law can be included by entering `nu` (from Table 3.2) as the *Dynamic Viscosity*, but in the case of a Maxwell rheology we have to use an additional Equation for Glen's flow law and therefore introduce `nupde` (see **Glen's flow law** below).

Table 3.2: Flow variables. Note that for two dimensional models COMSOL uses y and not z as vertical coordinate. Derivatives of the velocity in x and z direction are denoted by `ux` and `uy`.

name	expression	description
<code>nu</code>	$0.5 * E * (A)^{-1/n} * (d + 1e-30)^{((1-n)/n)}$	viscosity η (Eq. (2.8))
<code>d</code>	$\text{sqrt}(\max(\text{ux}^2 + 1/4 * (\text{uy} + \text{vx})^2, 1e-22))$	effective strain rate (Eq. (2.10))
<code>mismip_sl</code>	$-(C_const * (\text{abs}(-u * \text{ny} + v * \text{nx}) + 1e-30)^{(m-1)} * (\text{abs}(-u * \text{ny} + v * \text{nx})) * \text{test}(u * \text{ny} + v * \text{nx}))$	sliding law weak form

To incorporate the Maxwell model into the Laminar flow, we modify the equations generated by the physics node. Each physics node in COMSOL has an *Equation View*, in which the selected options and inputs are accessible as equations. We use that to change the computation of the stress to represent viscoelastic rheology. While in the Newtonian rheology the stress is given by $\tau = 2\eta \dot{\epsilon}^D$ (Eq. (2.5)), we want to include the stress of the Maxwell model, $\tau = \tau_E = 2G \epsilon_E^D$ (Eq. (2.13)). Hence we replace all occurrences of the viscous stress with the viscoelastic stress in the *Equation View*. To have an easy way to switch between the purely viscous and the viscoelastic case we implement a parameter `mw`, that is evaluated via *if*-statements and serves as a simple switch to select which

constitutive relation is used (see Fig. 3.4). This enables us to easily set up viscoelastic and purely viscous runs in the same model file.

Variables	
Name	Expression
spf.upwind_helpz	0
 spf.K_stress_tensorxx	if(mw==1,2*my*eps_xx_2_d,2*spf.mu*ux)
 spf.K_stress_tensoryx	if(mw==1,2*my*eps_xy_2_d,spf.mu*(vx+uy))
spf.K_stress_tensorzx	0
 spf.K_stress_tensorxy	if(mw==1,2*my*eps_xy_2_d,spf.mu*(uy+vx))
 spf.K_stress_tensoryy	if(mw==1,2*my*eps_yy_2_d,2*spf.mu*vy)

Figure 3.4: Replacement of the stress equations. In COMSOL notation my , $eps_xx_2_d$, $spf.mu$ are G , ϵ_E^D and η . Derivatives of v_x and v_z in x and z direction are denoted by ux and uy . The third component is zero, because we implement the model in two dimensions only. Yellow warning signs signify that the equations have been altered.

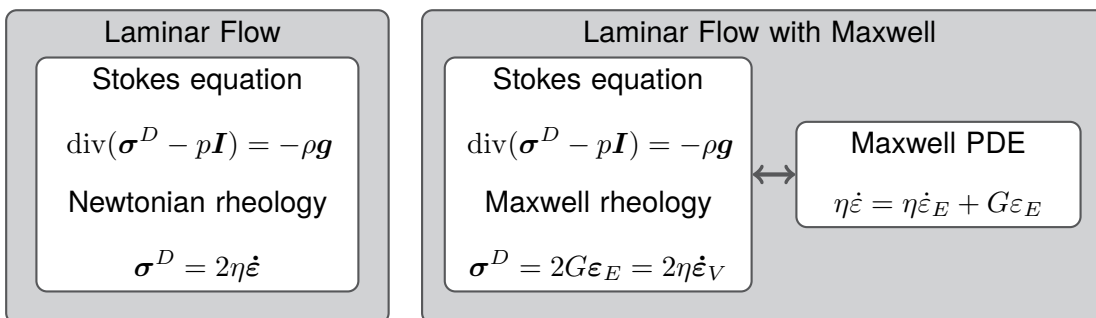


Figure 3.5: Default Laminar Flow compared to the modified version including Maxwell’s model.

Maxwell Model

The Maxwell model is implemented as a *Coefficient Form PDE*. This physics node can be used to implement arbitrary partial differential equations into COMSOL. Its default form is

$$e_a \frac{\partial^2 \mathbf{u}}{\partial t^2} + d_a \frac{\partial \mathbf{u}}{\partial t} + \nabla \cdot (-c \nabla \mathbf{u} - \alpha \mathbf{u} + \gamma) + \beta \cdot \nabla \mathbf{u} + a \mathbf{u} = f, \quad (3.1)$$

where \mathbf{u} is the dependent variable solved for. We set the coefficients to resemble our Maxwell equation for the deviatoric elastic deformation ε_E^D (Eq. (2.20)). This means all coefficient are set to zero, except for $a = G$ and $d_a = \eta$. The force term f is set to $\eta \dot{\varepsilon}^D$. Since we have three components ($\varepsilon_{E_{xx}}^D, \varepsilon_{E_{xz}}^D, \varepsilon_{E_{zz}}^D$), the PDE is a system of three equations:

$$\eta \frac{\partial \varepsilon_{E_{xx}}^D}{\partial t} + G \varepsilon_{E_{xx}}^D = \eta \frac{\partial v_x}{\partial x} \quad (3.2)$$

$$\eta \frac{\partial \varepsilon_{E_{xz}}^D}{\partial t} + G \varepsilon_{E_{xz}}^D = \frac{1}{2} \eta \left(\frac{\partial v_x}{\partial z} + \frac{\partial v_z}{\partial x} \right) \quad (3.3)$$

$$\eta \frac{\partial \varepsilon_{E_{zz}}^D}{\partial t} + G \varepsilon_{E_{zz}}^D = \eta \frac{\partial v_z}{\partial z}. \quad (3.4)$$

For the discretization we choose linear discontinuous Lagrange elements.

Glen's Flow Law

Although Glen's flow law is a simple explicit equation, we need to implement it in a way that allows us to solve it in a separate step as detailed in Section 3.1.4. Hence we add an additional *Coefficient Form PDE* and modify the coefficients to resemble an algebraic equation. The default form is the same as for the Maxwell model, Eq. (3.1), but in this case we only set $a = 1$ and therefore do not have any derivatives in the equation. The force term f is set to nu , which contains Glen's flow law from Eq. (2.8).

3.1.3 Boundary Conditions

Boundary conditions in COMSOL are added as subnodes to the corresponding Physics node. The dynamic boundary conditions are added inside the *Laminar Flow* node. COMSOL offers a set of predefined conditions which can be assigned to different edges of the geometry. It is convenient to group edges into named selections such as *surface*, *base*, *calvingfront* and *icedivide*. This is done in the *Definitions* and the resulting selections can also be used for generating the mesh and exporting the data.

To implement the kinematic boundary conditions we use COMSOL's *arbitrary Lagrangian-Eulerian* (ALE) method which has its own physics node. It handles the movement of boundaries with a combination of the *Lagrangian* method, where the observer (or mesh) moves with the material, and the *Eulerian* method, where the observer (or mesh) is fixed. This allows the boundaries to move without the need for the mesh to move with the material (COMSOL, 2012b, p. 908). This adds additional dependent variables X

and Υ , which the model has to solve for as well. For the discretization we choose linear elements.

Ice Surface

The ice surface is stress free (Eq. (2.26)) and we implement this in *Laminar Flow* as *Open Boundary* and add `surface` as the selection where the condition is applied to. For the kinematic condition (Eq. (2.24)) we add a *Prescribed Mesh Velocity* node to the *Moving Mesh* node and enter `u*nx+v*ny+smb` as prescribed velocity in vertical direction.

Ice Base

As discussed in the theory part, we have to determine if the ice base is in contact with the bedrock. Therefore we use a *Contact Pair* node (COMSOL, 2012b, p. 246) in *Definitions*. We choose the bedrock as source and the ice base as destination which gives us access to the `src2dst_ap1` operator that is equal to one if the selected edges are in contact with each other and zero otherwise. The search distance at which a point is considered to be in contact is set to 0.0001 m. As described in Section 2.3.2 we also compare the normal stress exerted by the ice to the water pressure to determine if the ice is afloat. In Table 3.3 the resulting variables are shown. Note that there is an additional variable

Table 3.3: Contact variables

name	expression	description
<code>sig_nn</code>	<code>rho_ice*g*(z_s-z_b)</code>	normal stress
<code>p_w</code>	<code>rho_sea*g*-(z_b-z_sl)</code>	water pressure
<code>contact</code>	<code>src2dst_ap1 && sig_nn > p_w</code>	
<code>contact_mesh</code>	<code>(src2dst_ap1 y<=b) && sig_nn > p_w</code>	

`contact_mesh` to check if the ice has penetrated into the bed.

For the bottom edge of domain I, where the ice is always in contact with the bedrock, we apply a *Slip Wall* condition, which implements $\mathbf{v} \cdot \mathbf{n} = 0$. Additionally we add the `mismip_sl` variable from Table 3.2 to the weakform in the equation view. This implements the sliding law directly in its weakform. This is necessary, because in its original form the *Slip Wall* condition applies a free slip condition. In *Moving Mesh* we set the *Prescribed Mesh Velocity* in x and y direction to zero, as the ice is not allowed to pass the bedrock, nor to move away from it. Additionally we add a *Pointwise Constraint* `0=-z_b+b` to this edge to get rid of numerical chattering between points. To apply a boundary condition depending on if the ice is in contact with the bed, we add a *Pairs* \rightarrow *Wall* node to domain II and III in *Laminar Flow*. Inside this node we add a *Fallback Feature* \rightarrow *Boundary Stress*. This way the *Slip* condition is applied where the ice is in contact while on parts without contact the fallback *Boundary Stress* with `-rho_sea*g*(y-z_sl)` is used. In the *Wall* node the `mismip_sl` variable is added to the weak expression as above, but only for parts where `contact` is true. For the kinematic

condition we use a *Prescribed Mesh Velocity* node and enter 0 for the x velocity and $\text{if}(\text{contact_mesh}, 0, -(u*nx+v*ny))$ for the y velocity. This is a good approximation of Eq. (2.27) and as above we add a *Pointwise Constraint* of $0=\text{if}(\text{contact_mesh}, -z_b+b, 0)$ for numerical stability.

Calving Front

The calving front is implemented according to Eq. (2.36). We use the *Boundary Stress* condition and enter $\text{if}(y<0, -\rho_sea*g*(y-z_s1), 0)$ as normal stress. Since the positions of the calving front is not allowed to change we add a *Prescribed Mesh Velocity* of zero in x -direction in the *Moving Mesh* branch.

Ice Divide

The boundary condition for the ice divide is given by Eq. (2.37). This is implemented as a *Symmetry* which is applied to the `icedivide` selection. Likewise the calving front, the ice divide does not move and the same *Prescribed Mesh Velocity* conditions is applied to it.

3.1.4 Solver

From all previous configuration steps COMSOL generates the FEM model equations which have to be solved to obtain a solution. There are a lot of strategies and methods to numerically find solutions to these equations. COMSOL provides a variety of *Solvers*, which approximate the numerical problem with a linearized problem and subsequently solve the resulting linear system of equations. We are interested in a prognostic solution and therefore use the *Time Dependent Solver*, which uses variable-step-size *Backwards Differentiation Formulas* (BDF) for the time derivatives, as described in Hindmarsh et al. (2005). The time step is not explicitly set, but adapted by the algorithm in respect to a given tolerance.

Since we have multiple variables to be solved, we need to decide if we use a *Fully Coupled Solver* or a *Segregated Solver*. While the *Fully Coupled Solver* solves for all variables at once, the *Segregated Solver* allows to define groups of variables which are solved for in separate steps. Variables not solved for in a particular step, are considered constant and values from the previous step are taken. The use of a *Segregated Solver* is usually used to reduce memory requirements, but in our case we need it in order to deal with the combined nonlinearity of Glen's flow law and the Maxwell model. We add two steps to the *Segregated Solver*. In *Segregated Step 1* the *Coefficient Form PDE* for Glen's flow law is solved. In *Segregated Step 2* the Stokes equations, the Maxwell equations and the equations for the ALE method are solved. In each step the system of nonlinear equations is solved with a damped Newton method. For each step we have to set an appropriate termination criterion. We end the iteration process if either a maximum of iterations n_{max} is reached or if the relative error is smaller than the relative tolerance. The relative error is given by the weighted Euclidean norm

$$\epsilon = \sqrt{\frac{1}{M} \sum_{j=1}^M \frac{1}{N_j} \sum_{i=1}^{N_j} \left(\frac{|E_{i,j}|}{W_{i,j}} \right)^2}, \quad (3.5)$$

where M is the number of fields (unknown variables solved for), N is the number of DOFs in field j and $W_{i,j} = \max(|U_{i,j}|, S_j)$. Here $U_{i,j}$ denotes the current approximation to the solution vector and S_j is a scale factor used to generate well posed matrices from variables of different magnitudes. The estimated error of $U_{i,j}$ is denoted by $E_{i,j}$ where the double subscript denotes DOF index (i) and field (j) component (COMSOL, 2012a, p. 940).

We set the relative tolerance to a value of 10^{-2} and the number of maximum iterations n_{max} in *Segregated Step 1* and *Segregated Step 2* to 100. For the outer loop around the two steps, we set $n_{max} = 20$. The complete solving process is pictured in Fig. 3.6. A *Stationary Solver* is used to obtain a initial solution from which the *Time Dependent Solver* is able to start.

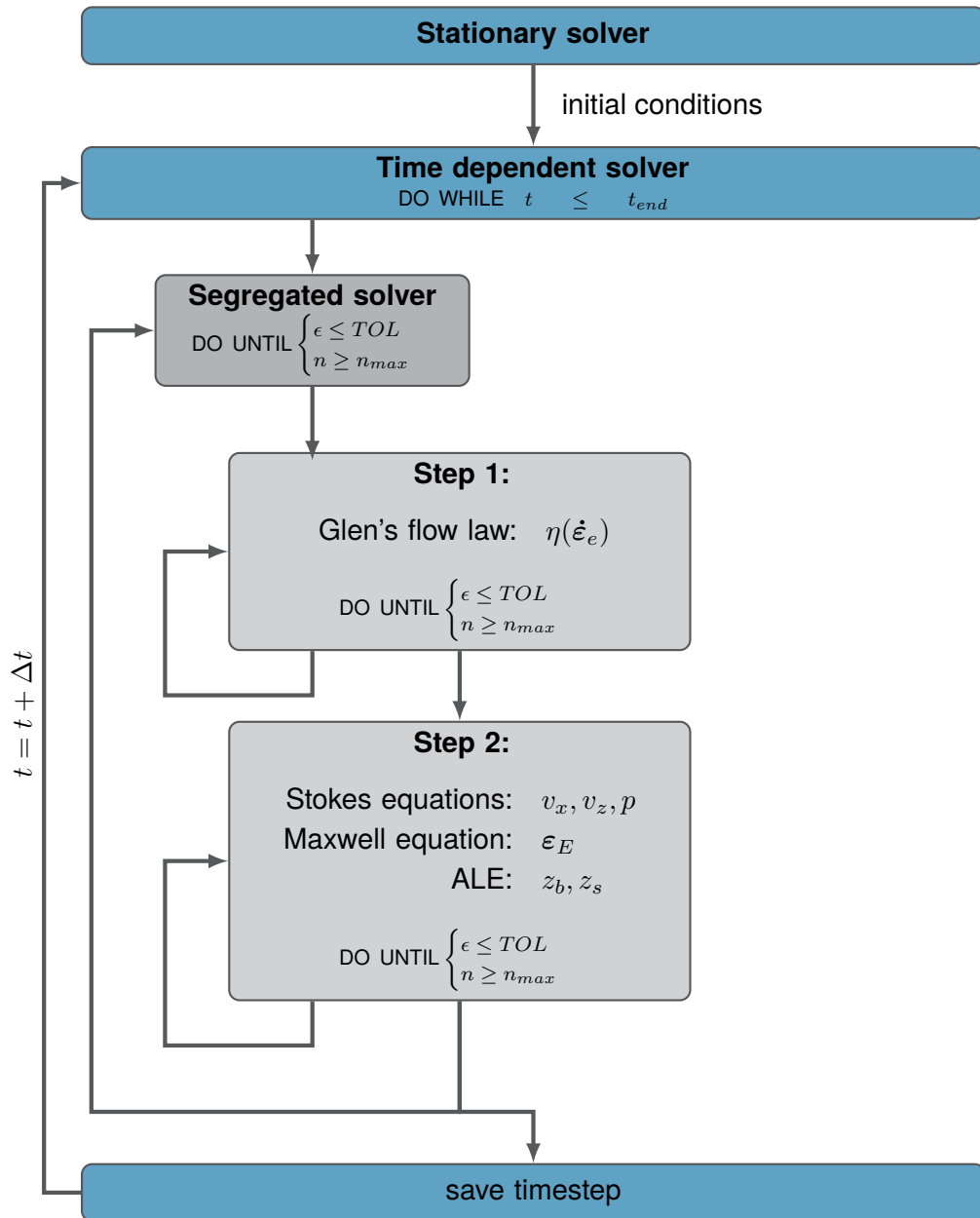


Figure 3.6: Solver sequence. The Stationary solver is identical to the time dependent setup without the loop over time and the computation for the ALE. It solves for a solution where all time derivatives are zero and this solution is used as initial condition for the time dependent solver.

3.2 Verification

A numerical model has to be tested before it can be used to make any projections. We distinguish between *verification* and *validation*. For the verification the model is tested in simple cases against analytical solutions and thus assures that the implementation is done correctly and the code contains no bugs. Validation can only be done when the verification was successful and aims to test whether the mathematical model sufficiently describes the real-world process it claims to represent. This can be done by comparing the model results to measured data. It is also possible to compare results from different models, a so called model intercomparison which is not clearly attributable to neither verification nor validation. In this thesis we only do the verification of our viscoelastic flow model.

As few viscoelastic ice models exist there is no well established benchmark or analytical solution yet. To verify our model we use two different setups. We check if the model is able to predict the correct longterm solution of iceflow with Glen's flow law with the *Ice Sheet Model Intercomparison Project for Higher-Order ice sheet Models* (ISMIP-HOM) (Pattyn et al., 2012). This is shown in Section 3.2.1. To test the viscoelastic behaviour we use a setup of stress build-up in a viscoelastic Maxwell body described in Gerya (2009), in Section 3.2.2.

3.2.1 ISMIP-HOM Experiment D

The Ice Sheet Model Intercomparison Project for Higher-Order ice sheet Models (Pattyn et al., 2012) is a set of six experiments for which the results of 28 models are compared. All results of the participating models are in close agreement and can therefore be considered as a reference. We implement experiment D: Ice stream flow II in our model to check if we can reproduce the longterm solution. Experiment D is a diagnostic experiment and therefore has no dependency on time. Since the longterm behaviour of the Maxwell model is identical to the behaviour of a Newtonian fluid, we can compare the solutions at a time t_{visc} where the elastic component has subsided completely. Ice shows elastic behaviour at timescales of hours, hence we choose $t_{visc} = 180$ d to ensure that only the viscous component drives the flow.

The geometry is given by

$$z_s(x) = -x \cdot \tan \alpha \quad (3.6)$$

$$z_b(x) = z_s(x) - 1000, \quad (3.7)$$

where $x \in [0, L]$ and $L = 160, 80, 40, 20, 10$ and 5 km and $\alpha = 0.1^\circ$. We only show the results for $L = 80$ km as they are representative for all lengths. It resembles an iceblock on an inclined bed with a constant ice thickness of $H = 1000$ m. The geometry and boundary conditions of Experiment D are shown in Fig. 3.7. The domain has lateral periodic boundary conditions, corresponding to infinite extend and no stress at the surface. At the base a sliding law in the form of Eq. (2.31) is applied, where the basal friction coefficient β^2 varies horizontally with x given by

$$\beta^2(x) = 1000 + 1000 \sin(\omega x), \quad (3.8)$$

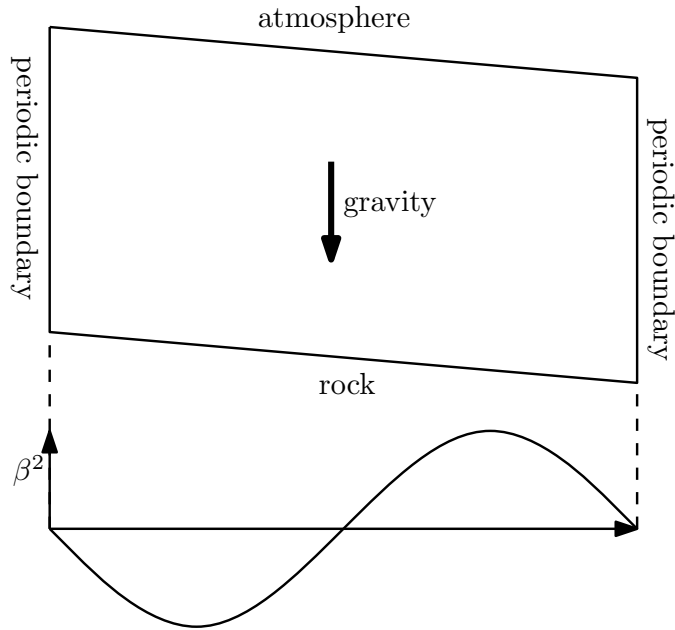


Figure 3.7: Geometry and boundary conditions of ISMIP-HOM Experiment D with basal friction coefficient β^2 .

with $\omega = 2\pi/L$. The ice flow parameters are given in Table 3.4. We compute the solution on a grid of 100×5 quadrilateral elements in x and z direction, resulting in 13 028 DOF.

Table 3.4: Flow parameters for the ISMIP-HOM Experiment D

name	expression	unit	description
rho_ice	910	kg m^{-3}	ice density
g	9.8	m s^{-2}	acceleration of gravity
A	10^{-16}	$\text{Pa}^{-3} \text{yr}^{-1}$	rate factor

In Fig. 3.8 the horizontal surface velocity is compared to the solution of the *mnr1* model from Pattyn et al. (2012). The *mnr1* model is also a full Stokes model implemented in COMSOL and therefore a logical candidate for comparison. The velocities produced by the Maxwell model agree well with the one given by the *mnr1* model. This shows the correct implementation of Glen’s flow law and the ability of the Maxwell model to represent secondary creep on long timescales.

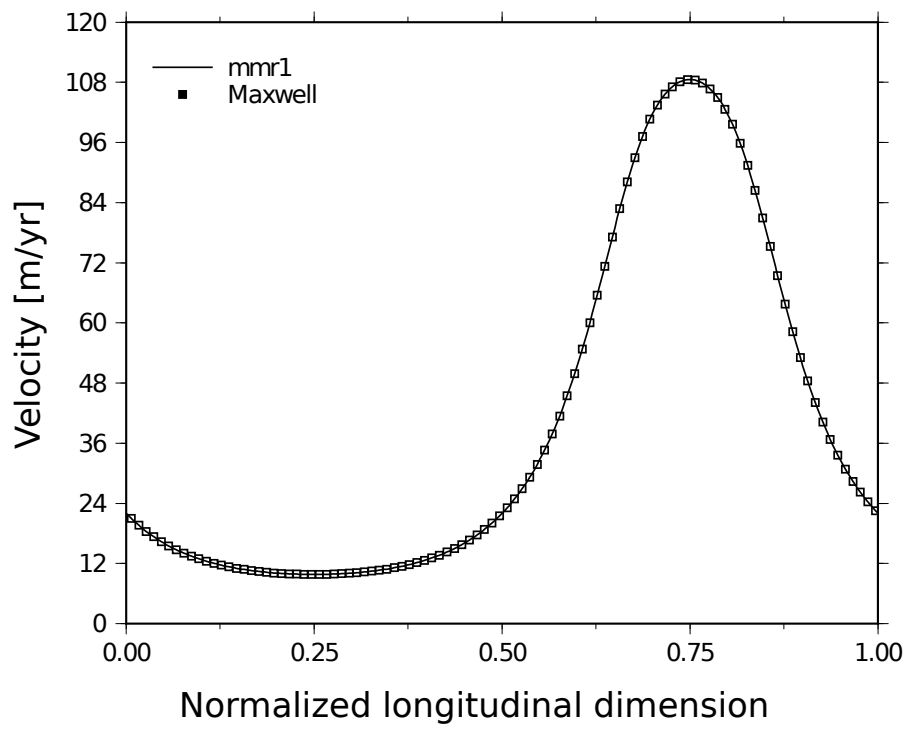


Figure 3.8: Comparison of horizontal surface velocities of the Maxwell model (symbols) and the mmr1 model (solid line) from Pattyn et al. (2012).

3.2.2 Stress Build-up in a Viscoelastic Maxwell body

For the case of uniform pure shear deformation of an incompressible viscoelastic medium under constant strain rate $\dot{\epsilon}_{xx}$, Gerya (2009) presents a solution for the deviatoric stress σ_{xx}^D given by

$$\sigma_{xx}^D = 2\dot{\epsilon}_{xx}\eta[1 - \exp(-tG/\eta)], \quad (3.9)$$

where η denotes the constant viscosity and G denotes the shear modulus. The material is initially unstressed. Based on Eq. (3.9) Gerya proposes a numerical test of stress build-up, which is pictured in Fig. 3.9. On a rectangular block constant velocities are prescribed at the edges, where v_x is pointed outwards from the vertical edges and v_y is pointed inwards from the horizontal boundaries. The velocities are given by

$$v_x = \frac{1}{2}\dot{\epsilon}L_x, \quad (3.10)$$

$$v_y = \frac{1}{2}\dot{\epsilon}L_y, \quad (3.11)$$

where $\dot{\epsilon}$ denotes the deviatoric strain rate and L_x and L_y the horizontal and vertical length of the block. There is no traction at the boundaries resulting in *free slip* conditions. We compute the solution for $\dot{\epsilon} = 10^{-14} \text{ s}^{-1}$, $\eta = 10^{21} \text{ Pa s}$ and $G = 10^{10} \text{ Pa}$ to be consistent with Gerya who is modelling the Earth's lithosphere. L_x and L_y are set to 1 m and discretized on a 25×25 quadratical element grid.

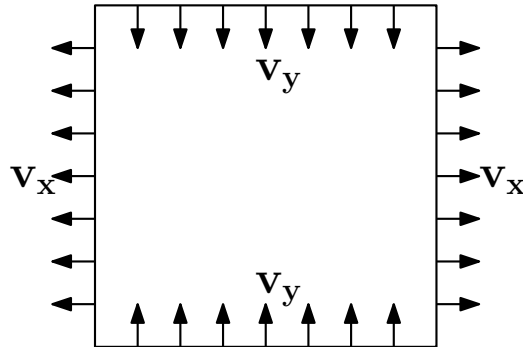


Figure 3.9: Setup for the stress build-up in a viscoelastic maxwell body.

Figure 3.10 compares the numerical solution to the analytical one and shows the high accuracy of the model. The numerical solution agrees well with the one given by Eq. (3.9) and therefore demonstrates the ability of the model to correctly describe the instantaneous elastic behaviour as well as the transition to the viscous regime.

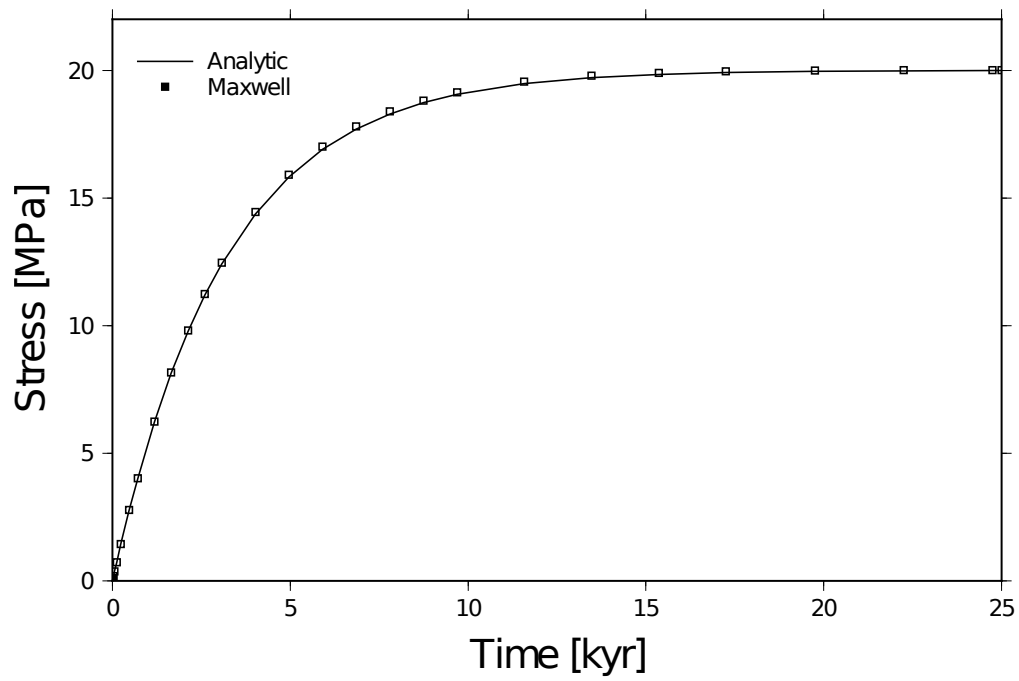


Figure 3.10: Comparison of analytic (solid line) and numerical (symbols) solution for viscoelastic stress build-up due to pure shear.

4 Experiments and Results

This chapter deals with the design and evaluation for the different experiments performed with the viscoelastic flow model. In Section 4.1 the experiment setups with their respective parameters are presented, while in Section 4.2 the results are shown.

4.1 Experiments

Tides arise from gravitational loading of various astronomical bodies. Due to the superposition of forces and frequencies, there is a vast amount of different resulting tidal constituents. Those, which are considered in our experiments, are given in Table 4.1. The focus of the experiments lays on determining the impact of the viscoelastic material model on the ice flow and grounding line behaviour. Therefore, we vary Young's modulus E , the amplitude A and the period T of the tidal forcing.

We divide the experiments into two major parts: In Experiment 1 (Section 4.2.1) we choose a relatively small amplitude which, due to the limited mesh resolution, does not trigger any migration of the grounding line. In Experiment 2 (Section 4.1.2) we choose a high amplitude, which leads to a migration of multiple mesh elements. This enables us to study the effects of the viscoelasticity separately from the grounding line migration.

Table 4.1: Tidal constituents used in the experiments

Name	Symbol	Period in hours
Principal lunar semidiurnal	M_2	12.420
Principal solar semidiurnal	S_2	12.000
Lunisolar synodic fortnightly	M_{sf}	354.367
Lunar monthly	M_m	661.311

4.1.1 Experiment 1: No migration M_2 S_2 tide

Experiment 1 aims to study the effect of the viscoelastic material model on the ice flow. We use the geometry described in Section 3.1.1 with an inclination of the bed given by $s = 1/1000$. The grid spacing in the vicinity of the grounding line H_{min} is 150 m. At the ice divide the spacing is $H_{maxI} \approx 20$ km and $H_{maxIII} \approx 10$ km at the calving front. The model is forced with a superposition of the M_2 and S_2 tidal components each with an amplitude of 0.3 m. Therefore, the maximum amplitude is 0.6 m, which is not enough to

trigger grounding line migration at the given grid resolution. These values can be seen as realistic for some ice shelves, although tidal amplitudes vary strongly with geographical location. In this experiment the grounding line is always located at $x = 546875\text{m}$.

We vary Young's modulus over three values as given in Table 4.2 and also do a purely viscous reference run.

Table 4.2: Values for Young's modulus used in Exp. 1 and their respective solution times.

Young's Modulus in Pa	Solution time
purely viscous	18 hours
1.4×10^{10}	3 days, 1 hour
5.0×10^9	1 day, 21 hours
1.0×10^9	2 days, 18 hours

Motivated by the study of Gudmundsson (2011) we varied the exponent in the sliding law m and conduct this experiment with a nonlinear sliding law, setting $m = 1/3$ (this corresponds to $m = 3$ in the study of Gudmundsson, due to alternative formulation of the equation), as well as with linear sliding with $m = 1$. For the $m = 1$ case we additionally changed the sliding parameter C to $2 \times 10^{10} \text{ Pa m}^{-1} \text{ s}^{-1}$. This ensures that the observed velocities will be in comparable range.

The experiment is performed over a period of 90 days and the variable time step is constrained by a minimum of one step every ten minutes for the purely viscous run. Results of Experiment 1 are shown in Section 4.2.1.

4.1.2 Experiment 2: High amplitude, M_m tide

In Experiment 2 we want to investigate the effect of tides and the viscoelastic rheology on grounding line migration. Since the amplitudes used in Experiment 1 are too small to induce the migration, we choose an amplitude of 10 m for Exp. 2. While such a high amplitude is unrealistic, it enables us to study the effect in general.

We use the same geometry as in Exp. 1, which is $s = 1/1000$, $H_{min} = 150 \text{ m}$, $H_{maxI} \approx 20 \text{ km}$ and $H_{maxIII} \approx 10 \text{ km}$. For the tidal constituent we choose a much longer period because a large displacement over short time would likely result in numerical instability. Hence we pick $T = 30 \text{ d}$, which is close to the M_m constituent.

We are also interested in the influence of the bedrock inclination and therefore, we repeat the experiment with a new geometry, in which s is set to $1/500$. Results are presented in Section 4.2.2.

4.2 Results

4.2.1 Experiment 1

In Fig. 4.1 the horizontal surface velocities at various distances upstream of the grounding line are shown for the purely viscous (a) and the $E = 1.4 \times 10^{10} \text{ Pa}$ (c) case. Linear trends

have been removed and the signal has been normalized by dividing it by its maximum. We show an extract from day 66 to day 81, which corresponds to one tidal cycle of the superimposed M_2 and S_2 constituents. Over the whole duration of the experiment (90 d) we obtain 4 complete cycles, but since they are extremely similar to the one in Fig. 4.1 we do not show them here.

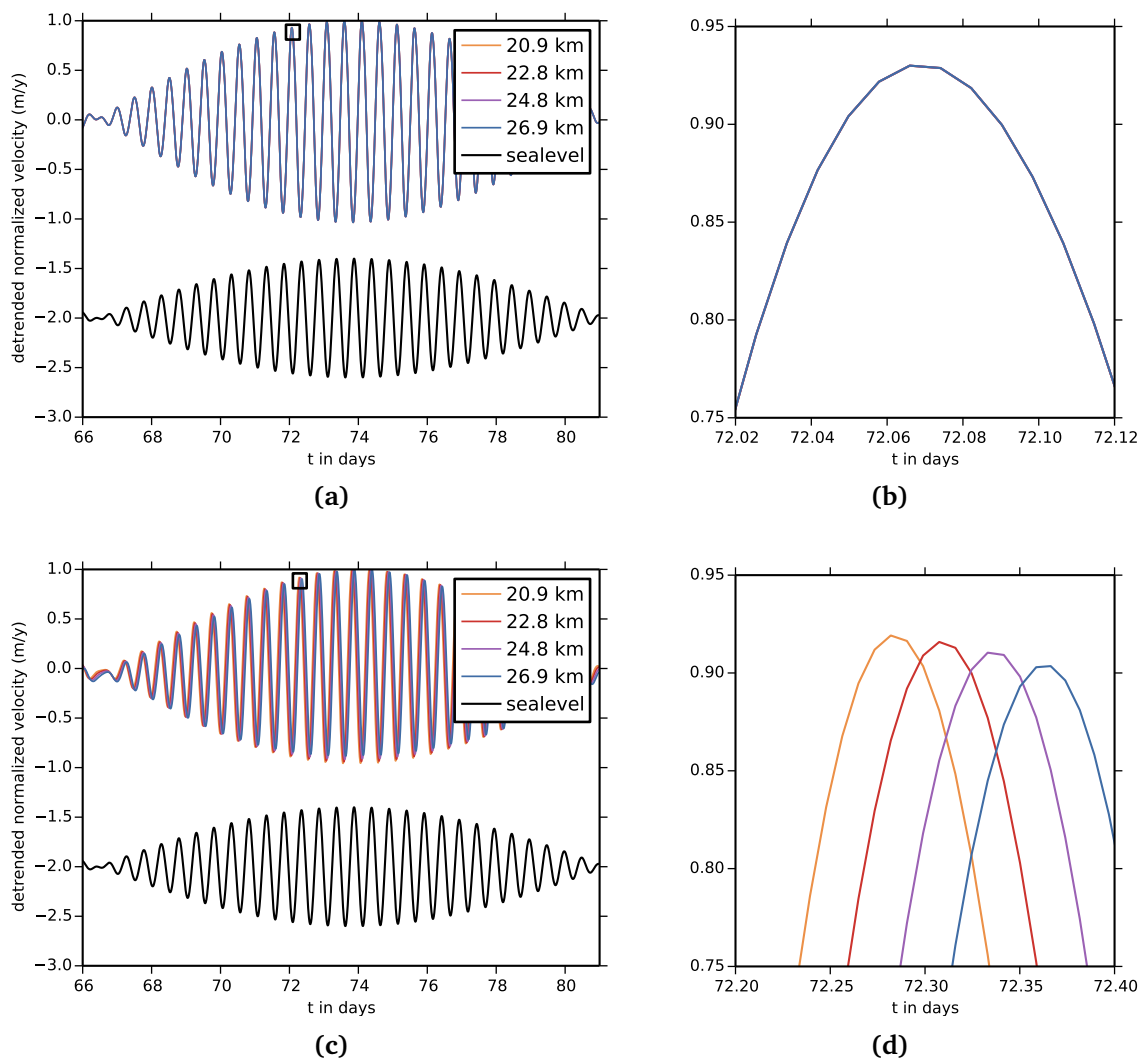


Figure 4.1: Horizontal detrended and normalized velocities at different distances to the ground-line. The sea level (black) is shifted by -2 m along the y-axis.

(a) Purely viscous reference run.

(b) Closeup of a local maximum from (a). No phase shift visible.

(c) Maxwell model with $E = 1.4 \times 10^{10}$ Pa.

(d) Closeup of a local maximum from (c). The Maxwell model causes a phase shift.

It is obvious that the ocean tides modulate the flow of the ice in the case of a purely viscous as well as in the case of a Maxwell rheology. For the purely viscous case we directly observe high velocities at low tides and low velocities at high tides. For all observed positions, from 20.9 to 26.9 km upstream of the grounding line, the velocities are identical (see also the closeup in Fig. 4.1(b)). For the Maxwell case, shown in Fig. 4.1(c), however, we find a phase shift in the velocities (clearly visible in the closeup Fig. 4.1(d)).

At larger distance from the grounding line the shape of the velocity signal changes. In Fig. 4.2 the detrended and normalized velocity at a distance of 87 km inland from the grounding line is presented. The velocity is barely correlated to the tidal signal but we

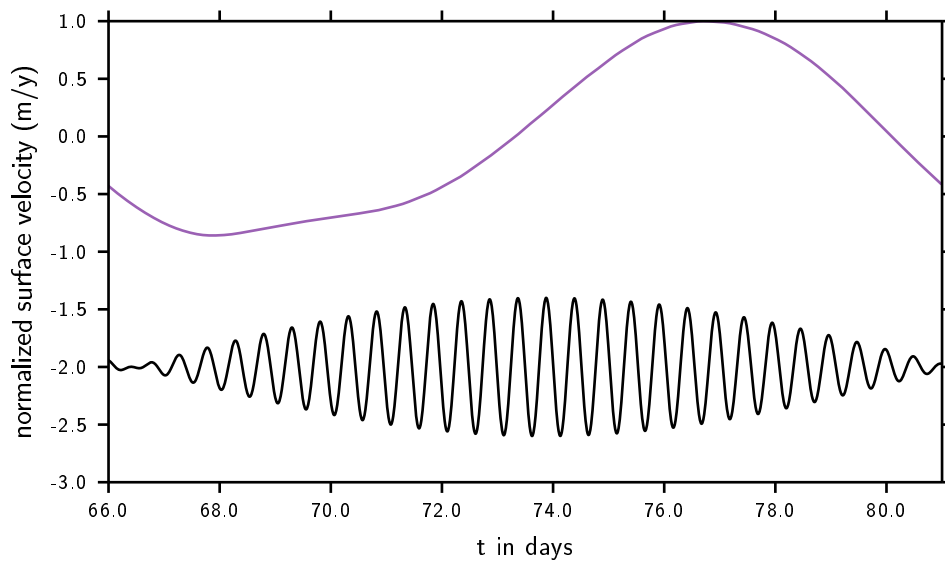


Figure 4.2: Horizontal detrended and normalized surface velocity at a distance of 87 km upstream of the grounding line. The velocity modulation takes place at a long tidal period close to the M_{sf} period.

notice a modulation of the flow velocity with a period close to the fortnightly period of the M_{sf} tidal constituent.

In an ice sheet – ice shelf system the surface velocity increases towards the sea, due to the fact that the ice is allowed to float freely on the water. This is also true for flow modulations arising from tides. Figure 4.3 shows the maximum of the detrended horizontal surface velocity at various distances to the grounding line. This allows us to study how the amplitudes of the flow variation are affected by the elastic parameter E .

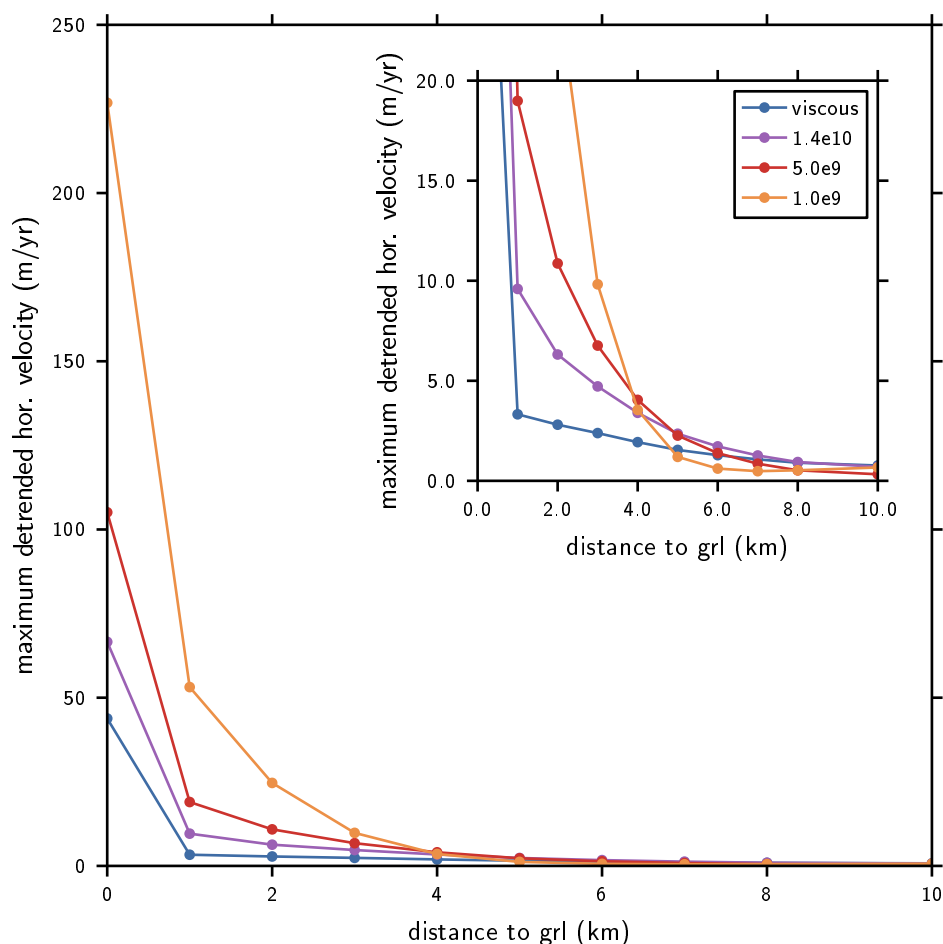


Figure 4.3: Maximum of the detrended horizontal surface velocity over the distance to the grounding line for various elastic parameters. The viscous reference is shown in blue, $E = 1.4 \times 10^{10}$ Pa in purple, $E = 5 \times 10^9$ Pa in red, and $E = 1 \times 10^9$ Pa in yellow.

As predicted, the amplitude decreases with the distance to the grounding line. Smaller ('softer') elastic parameters cause higher amplitudes at the grounding line, while the purely viscous reference produces the lowest velocity. A close inspection of the closeup reveals that the velocity decays faster with distance for smaller elastic parameters. At a distance of 4 km the maximum velocity produced by the softest model, is already lower than the velocity of the model with $E = 5 \times 10^9$ Pa.

The flux q over the grounding line is a crucial quantity for the mass balance and also the grounding line position. It is given by

$$q = \overline{v_x}|_{x_{grl}}(z_s - z_b)\rho_{ice}, \quad (4.1)$$

where $\overline{v_x}|_{x_{grl}}$ denotes the vertical mean horizontal velocity at the grounding line. In Fig. 4.4 the flux is presented for different values of Young's modulus over one tidal cycle.

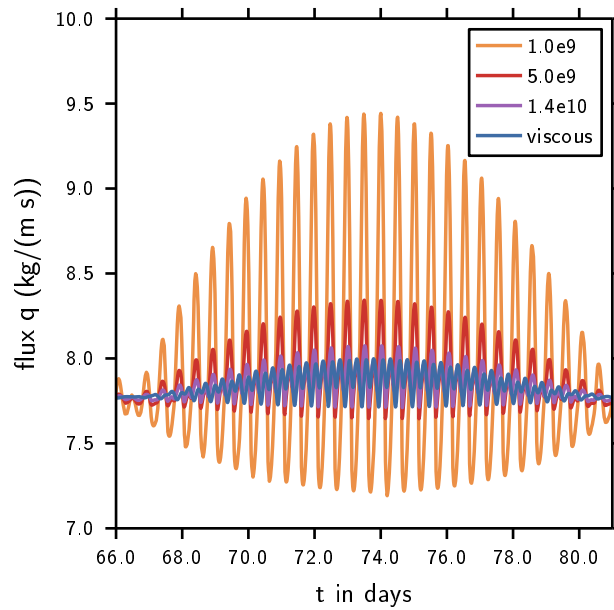


Figure 4.4: Flux across the grounding line for different elasticity parameters. Smaller elastic parameters lead to increased flux.

We observe a significant asymmetry of the flux, which leads to an increase in the mean flux. The flux also strongly depends on the Young's modulus. A smaller value for E leads to increased flux, while the purely viscous reference shows the lowest flux.

To determine if the increase in mean flux depends on the forcing, we repeat the experiment with a tidal period of $T = 30$ d as in Exp. 2 without viscoelasticity. The experiment is done over a period of 180 days. All other parameters stay the same. In Fig. 4.5 the resulting flux for this case is shown.

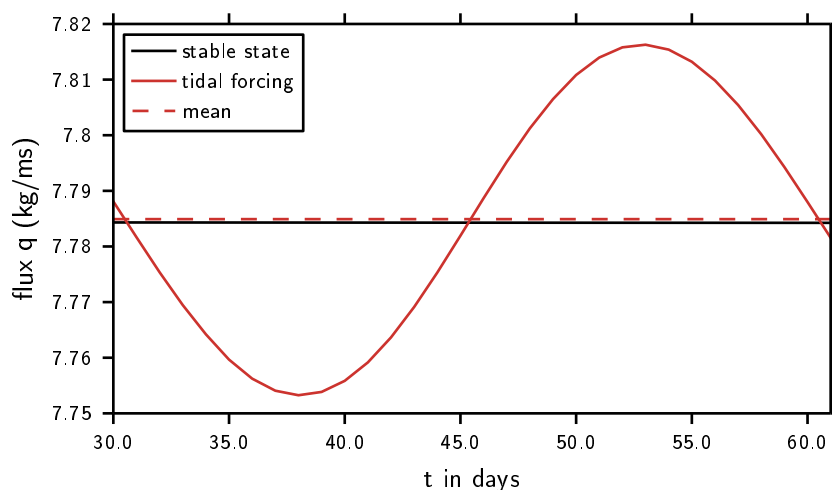


Figure 4.5: Flux across the grounding line for a tidal period of $T = 30$ d (red line) and purely viscous material model compared to the steady state flux (black line). The mean flux of the tidally modulated model (dotted red line) is slightly higher than the steady state flux.

While not as obvious as in the previous case, the asymmetry still exists. The mean flux for the tidally modulated is slightly higher than the steady state flux.

In Fig. 4.6 and Fig. 4.7 the results for different sliding laws are presented. Figure 4.6 shows normalized detrended surface velocities at five different points between 0 and 43 km upstream of the grounding line for the nonlinear sliding law using $m = 1/3$. Herein we observe a noticeable asymmetry directly at the grounding line, which is not present 10 km upstream. At a distance of 20 km the asymmetry is barely visible, but it clearly reappears at 30 km and is even more prominent at 43 km.

For the case of the linear sliding law ($m = 1$) the behaviour is similar. It is shown in Fig. 4.7. At the grounding line we observe strong asymmetry, while at a distance of 10 km the signal is almost symmetrical. With increasing distance from that point, the asymmetry increases again.

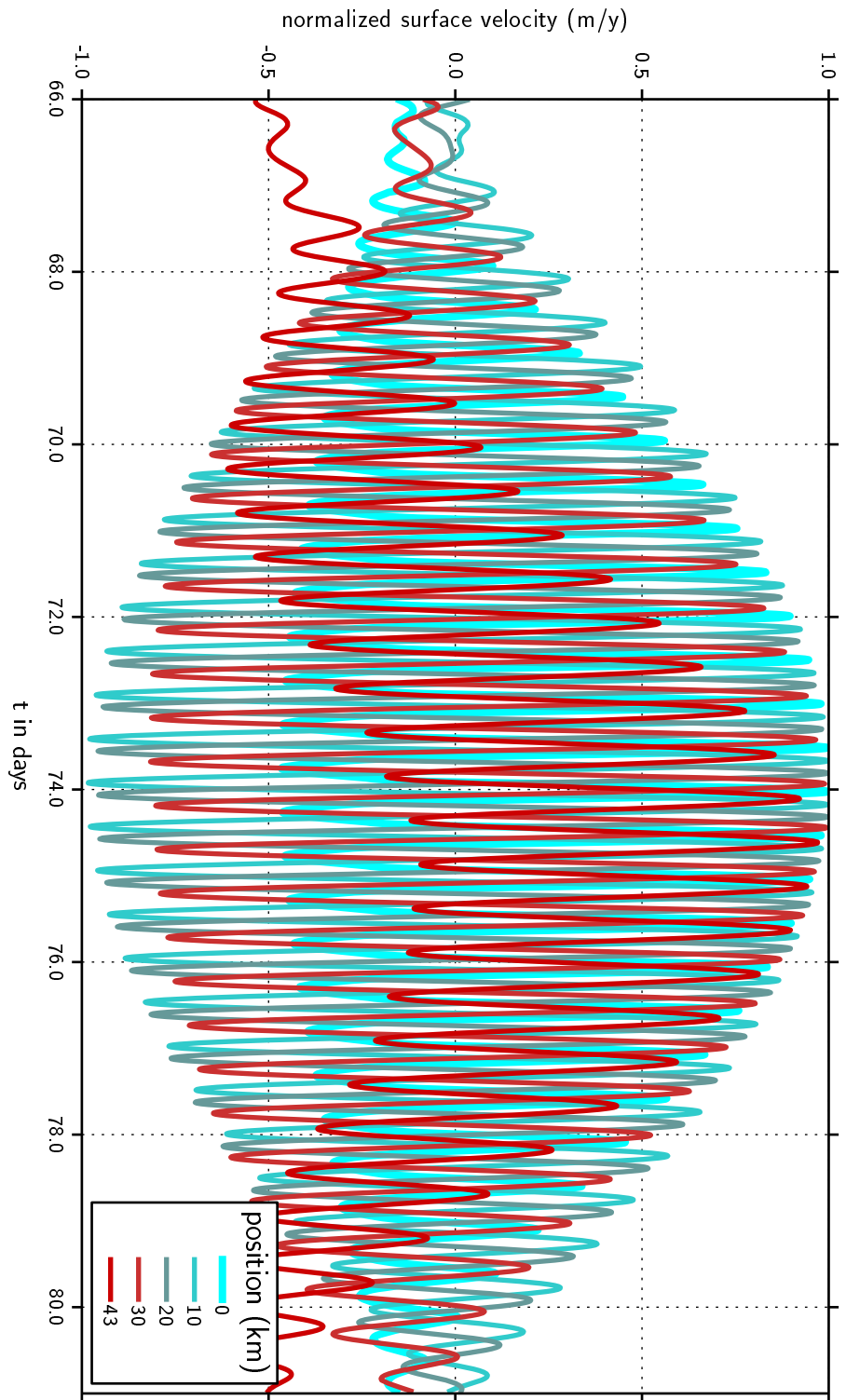


Figure 4.6: Normalized detrended horizontal surface velocity at various distances from the grounding line for the case of $m = 1/3$.

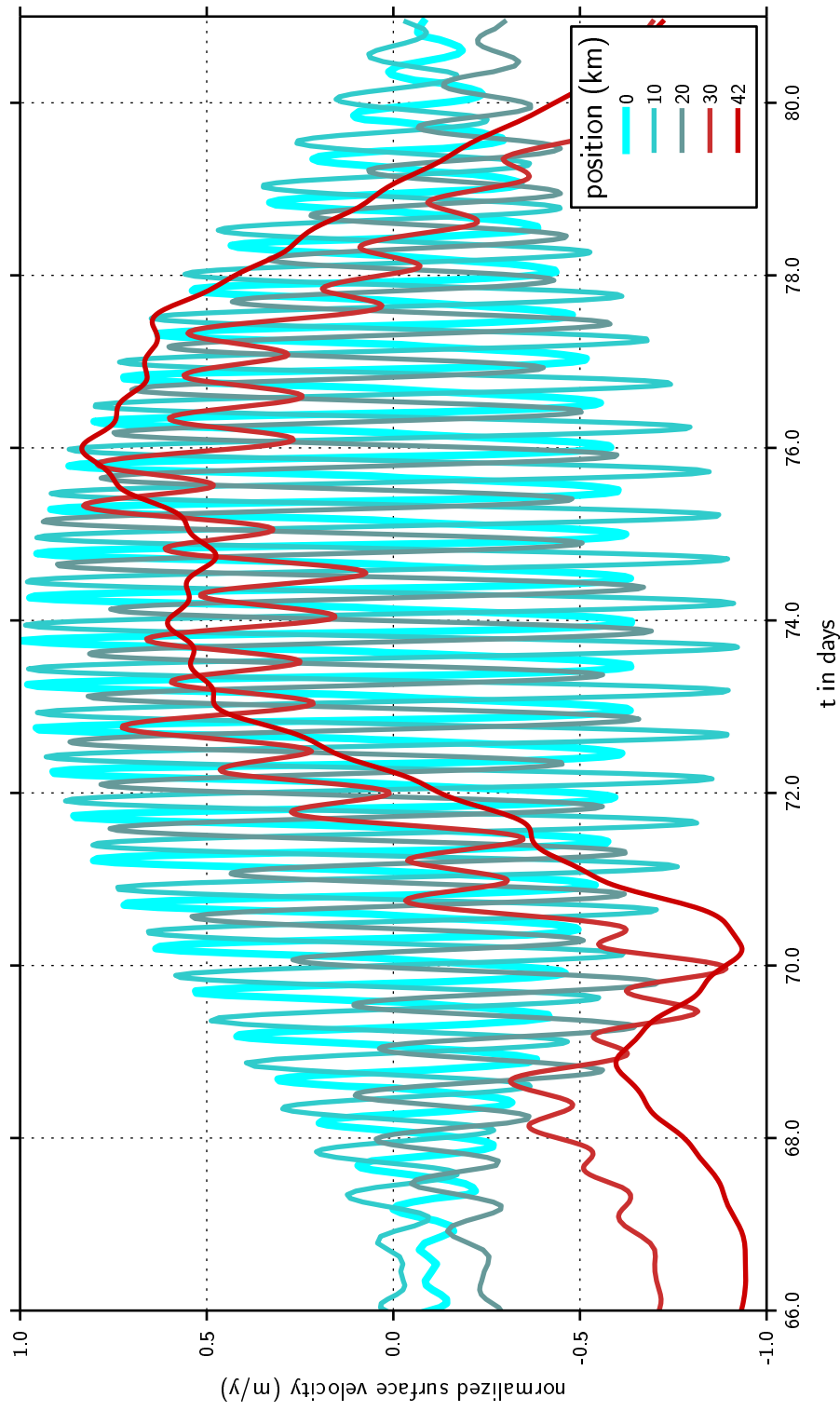


Figure 4.7: Normalized detrended horizontal surface velocity at various distances from the grounding line for the linear sliding law $m = 1$.

4.2.2 Experiment 2

In Fig. 4.8 the results for Exp. 2 are shown for two different values of Young's modulus. While in Exp. 1 high tides correspond with low velocities, the relation is more complex here due to the migrating grounding line. We observe a sinusoidal velocity modulation, which is similar to the one in Exp. 1. The velocity decreases when the sea level rises. But this sine-shaped modulation is disrupted by 'jumps', which counteract this behaviour. They are caused by the migration of the grounding line. Whenever the grounding line advances by one element, the velocity drops.

Retreat of elements leads to an overshoot in the velocities. This is clearly visible for the case of $E = 5 \times 10^9$ Pa but also present for $E = 1.4 \times 10^{10}$ Pa, although with much smaller amplitudes. Each overshoot decays after approximately 3 h for the 1.4×10^{10} Pa and after approximately 5 h for the 5×10^9 Pa case. For the advance of the grounding line, no overshoot is observed.

The grounding line position over time does not depend on the elastic parameter in this case. Both models show the same advance and retreat. Over the observed 180 days the grounding line shows a general trend to retreat, when compared to the steady state position. Accordingly the velocity is generally increasing over the whole observation period.

The results of the same experiment with the shallow bedrock are presented in Fig. 4.9. The behaviour is very similar to the one in the previous geometry. The relation between velocity and tide is visible even better, due to the lack of overshoot. While the grounding line on the previous geometry migrates mostly over 5 elements (750 m) for one cycle, it only migrates over 3 elements (450 m) in the shallow geometry. At 130 days the grounding line retreats one element further in purely viscous model than in the viscoelastic model, but we consider this a numerical artifact.

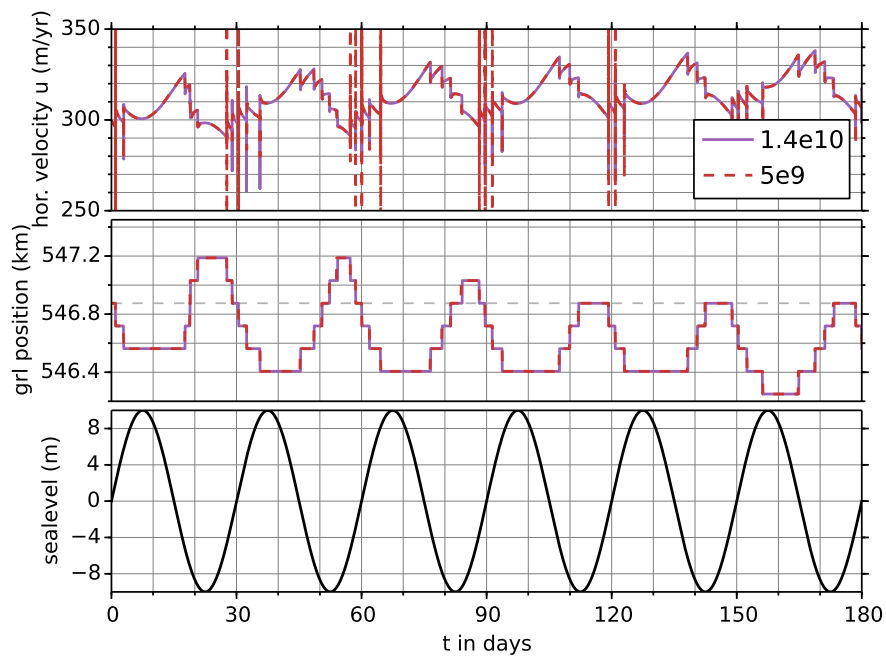


Figure 4.8: Results for Exp. 2 at a distance of 6 km upstream. The upper panel shows the velocities for $E = 5 \times 10^9$ Pa (purple line) and $E = 1.4 \times 10^{10}$ Pa (red dashed line). In the middle panel the position of the grounding line is shown and the bottom panel contains the sea level.

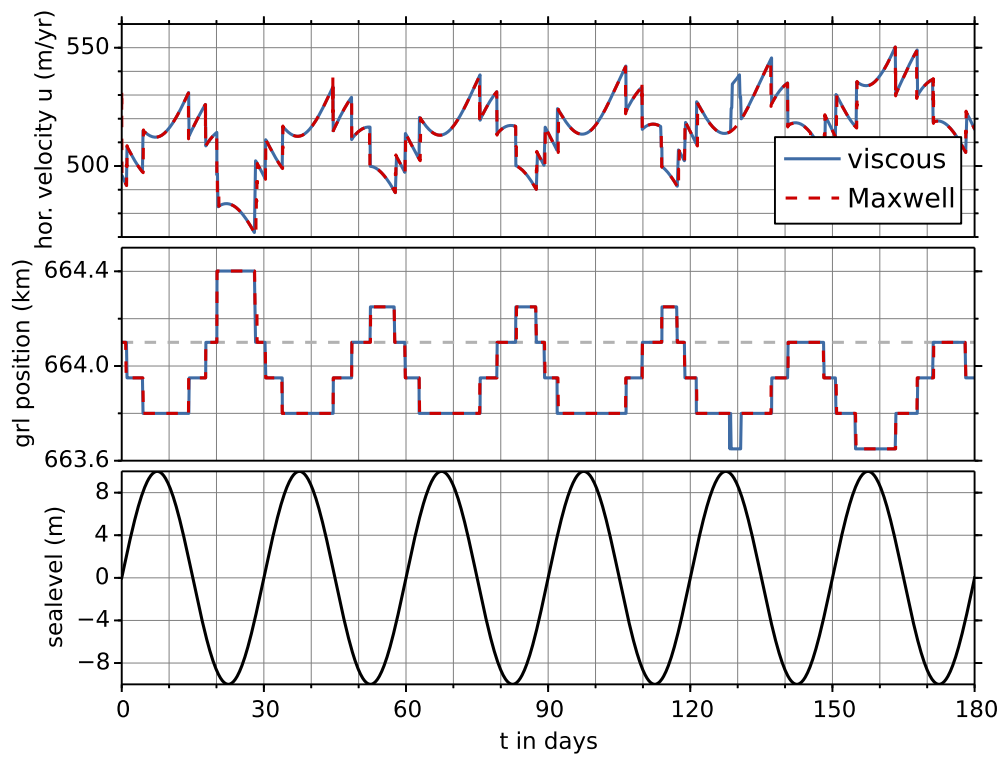


Figure 4.9: Results for Exp. 2 at a distance of 6 km upstream for a shallower geometry with $s = 1/500$. The viscous case is compared to the Maxwell case with $E = 1.4 \times 10^{10}$ Pa.

4.3 Discussion

4.3.1 Experiment 1

In Experiment 1 we observe a significant phase shift in the velocities, which is not present in the purely viscous case (Fig. 4.1). This can be explained by the fact that the Maxwell material model, in contrast to the purely viscous rheology, contains time derivatives. Therefore perturbations propagate with finite velocity. A phase lag to oscillatory forcing is in fact a classic characteristic of a viscoelastic material (Findley et al., 1976). This phase shift has already been observed in GPS studies of ice shelves (e.g. Lohse, 2012). A combination of GPS surveys (or remote sensing data) with appropriate models can be used to constrain *in situ* viscoelastic properties of ice.

The shape of the velocity signal varies with the distance to the grounding line. At close distance, the velocity resembles the tidal forcing and the frequency of the velocity matches the frequency of the forcing. At larger distances the signal is transformed, higher frequencies are dampened and at a distance of 87 km we observe a frequency which corresponds to the M_{sf} tidal constituent, which is not present in the forcing (Fig. 4.2). This may seem surprising, but it is a basic property of a nonlinear system. While a linear system can only produce responses at the frequency range it has been forced at, a nonlinear system is not subjected to the superposition principle and may therefore, produce a response at a different frequency. The S_2 and M_2 tidal constituents produce a nonlinear interaction which leads to flow perturbations at frequencies not previously present in the forcing. Gudmundsson (2011) observes this behaviour as well and attributes it to the nonlinear sliding law, which we can not confirm in our study (see below).

We observe a relation between Young's modulus E and the detrended velocity amplitudes. A smaller elastic parameter produces higher amplitudes at the grounding line. At a certain distance this relation is inverted and the model with the smallest elastic parameter shows the smallest amplitudes (Fig. 4.3). This is also an effect of the Maxwell material model. It can be pictured like this: Sudden stress on the Maxwell unit immediately deforms the spring, while the damper reacts more slowly. A smaller elastic parameter implies a softer spring which leads to large velocities at the grounding line. A softer spring also absorbs more of the stress, while a stiffer spring transfers more stress to the damper. Hence for larger elastic parameters the energy is transported further into the ice sheet and leads to higher amplitudes further upstream.

This is also the explanation for the dependency of the flux to the Young's modulus, because it depends mostly on the velocity. For the mass balance and long term position of the grounding line this would not be relevant, since higher amplitudes do not change the mean of the flux, but due to the strong asymmetry (Fig. 4.4), we observe an increase in the mean flux. This asymmetry is also present when the model is forced with a single period of $T = 30$ d (Fig. 4.5). It is therefore not a result of the nonlinear

interaction of tidal constituents, but a direct result of the nonlinearity of the system. The flux variation is driven by the variation of the velocity at the grounding line, since the ice thickness does not change over the observed period. Since the flux across the grounding line determines its advance or retreat behaviour (increased flux correlates with retreat and decreased flux correlates with advance), this has important implications.

In Table 4.3 the differences of the temporal mean of the flux $\Delta\bar{q}$ are shown for different elastic parameters. We observe a difference of 0.77 % for the purely viscous case, which means that the behavior is not exclusively an effect of the viscoelasticity. Though viscoelasticity amplifies the effect and for a Young's modulus of 1×10^9 Pa we obtain a difference of 3.57 %. This means, that by not including tides and viscoelasticity in ice models, we commit a significant error.

Table 4.3: Comparison of the temporal mean flux \bar{q} over the grounding line for different elastic parameters. The difference between the steady state flux and the flux in the tidally forced case is denoted by $\Delta\bar{q}$.

	\bar{q} in $\text{kg m}^{-1} \text{s}^{-1}$	$\Delta\bar{q}$ in $\text{kg m}^{-1} \text{yr}^{-1}$	$\Delta\bar{q}$ in %
steady state	7.784	–	–
purely viscous	7.844	0.060	0.770
$E = 1.4 \times 10^{10}$ Pa	7.872	0.088	1.131
$E = 5 \times 10^9$ Pa	7.925	0.141	1.805
$E = 1 \times 10^9$ Pa	8.062	0.278	3.567

Gudmundsson (2011) also describes asymmetries in the velocities and attributes them to the nonlinear sliding law. In his reference experiment with linear sliding ($m = 1$) no asymmetry occurs. This contradicts our findings, that the behaviour for $m = 1/3$ and $m = 1$ is basically the same and the shape and symmetry differs with the location of observation. While our modelling approaches are similar, there are some important differences, which can possibly cause the disagreement in our findings.

The geometry in the model of Gudmundsson spans 170 km and has a different bedrock slope upstream (0.003) and downstream (0.001). Our model geometry has a horizontal extension of 800 km and the slope is 0.001 for the whole domain. While Gudmundsson uses an *Upper Convected Maxwell* (UCM) material model, which is a generalization of the Maxwell model for large deformations, we chose a Maxwell model, since we only deal with small deformations. We also neglect compressibility of the ice, while Gudmundsson includes it in the elastic part of his model. The major distinction is in the handling of the boundary conditions. In Gudmundsson's model the boundary positions are merely fixed and only the ice sheet is allowed to move according to the tides. In our model we consider the entire ice base and ice surface and implement movement corresponding to the flow dynamics.

Apparently we are observing an additional nonlinearity, which is not caused by the sliding law. The complete explanation for the disagreement has not yet been found and demands further investigation of the problem.

4.3.2 Experiment 2

The results of Experiment 2 show that our model is able to realise a grounding line migration using a viscoelastic material model. In Fig. 4.9 we can observe the relation between the tides, the grounding line positions and the flow velocity in detail. At high tide the grounding line is at its position farthest upstream (minimum) and the velocity is at maximum. The grounding line is only able to migrate in distance increments prescribed by the grid size, which leads to the discontinuous movement. A close inspection of the velocity shows, that we deal with a sinusoidal shape, which is disrupted by sudden 'jumps' occurring whenever the grounding line advances or retreats by one element. This sine wave has its minimum when the sea level is at maximum. This sine wave is however dissected and offset, such that the maximum velocity occurs at the maximum tide. This reveals that the velocity modulation induced by the ocean tides is not as simple as described in the introduction, but the result of two different processes. As described in the introduction, the uplifting of the ice shelf leads to landward movement of the grounding line. Therefore, less area is in contact with the bedrock and affected by basal stress. This results in higher velocities at high tides. The discontinuous movement of the grounding line causes this process to cause the 'jumps' in the flow velocity.

Additionally there is another process which is the normal stress directly exerted by the sea on the ice body as a boundary condition. This stress increases at high tide, according to Eq. (2.34), reduces the flow velocity and therefore counteracts the uplifting effect. In the presented experiments the effect of the migrating grounding line dominates, but this likely depends on various factors, such as geometry and tidal amplitude.

The overshooting of the velocity, seen in Fig. 4.8, is a typical response of the Maxwell model to a sudden change in the boundary conditions. The decay times are reasonable for the respective elastic parameter. Interestingly the overshooting only occurs when the grounding line is retreating. While during an advance, no overshooting is visible. For the shallow geometry we do not notice any overshooting at all.

When we compare the movement of the grounding line for the Maxwell and the purely viscous case, there is practically no difference. Viscoelasticity does not have an influence on the migration of the grounding line in our experiment. We explain this with the relatively long periodical forcing, which happens on a timescale where the dominant rheological behaviour of ice is already purely viscous and expect measurable differences for tidal constituents of smaller periods.

Over the whole duration of the experiment we notice a general retreat of the grounding line. It migrates back and forth over a few elements and the time spent at the position farthest upstream increases with each cycle and does not reach its previous maximum until it migrates one element further in upstream direction. This implies that the inclusion of tides possibly leads to a new equilibrium state of the system.

In the variant of Exp. 2 with the shallow bed, the grounding line migrates over a smaller distance. This is a surprising result, because the assumption is that at a less

inclined bed the same tidal amplitude, results in a larger grounding line migration. Here we have to consider that the shallow bed results in a totally new equilibrium position and a lot of other factors have also changed. Nevertheless this experiment suggests, that there is a more complex relation between the bedrock inclination and migrated distance.

5 Conclusion and Outlook

In this thesis we investigated the role of tides in the dynamics of ice sheet – ice shelf systems. Therefore, a full Stokes viscoelastic ice model has been developed and implemented. We discuss implications of different rheological models and chose a Maxwell model to represent the rheological behaviour of glacier ice, based on that discussion. The flow model is tested against results from the ISMIP-HOM benchmark (model intercomparison) and against a pure shear setup, for which an analytical solution is available. In both test cases our flow model performs extremely well, being able to reproduce elastic properties on short timescales, as well as long term viscous creep. The solutions agree well even in the transition zone between the elastic and viscous regime. This provides confidence that the implementation is done correctly and that allows applying the model to study the influence of tides on the ice flow.

We are especially concerned with the processes at the grounding line, since it is the most crucial point for determining the mass flux of the system. The mass flux controls contribution to sea level rise and the general stability of the ice body. Tidally induced migration of the grounding line has been observed but the exact processes are not yet fully understood. Therefore, we performed various experiments on an idealized ice sheet – ice shelf geometry to improve our understanding of the system. From the results obtained we can draw the following conclusions:

Ice stream flow velocities are clearly modulated by tidal forcing. For the Maxwell model we find a phase shift in the horizontal velocities upstream the grounding line. Additionally we find a significant velocity variation with a period close to the M_{sf} period of 14 days, even though we force the system with the S_2 (12 h) and M_2 (12.42 h) tidal constituents. This is a result of the nonlinear interaction of the forcing and the system response, which is not present in purely viscous models. These effects have also been observed at ice shelves and ice streams in Antarctica.

The amplitude of velocity variations at the grounding line depends strongly on the elastic parameter. While smaller values for Young's modulus produce larger amplitudes close to the grounding line, they also cause them to decay more rapidly with distance. Further upstream from the grounding line larger elastic parameters produce larger amplitudes. This means, that we deal with a dampening effect, which controls how far upstream into the ice shelf tidal energy is transported. The exact implications of this are still unclear and have to be addressed in further studies. In connection with the phase shift this knowledge may possibly be used to determine material parameters from

satellite or GPS data.

For the mass balance of glacier system the flux across the grounding line is a key quantity. It is a measure of how much mass is lost by the ice sheet and contributes to sea level rise, and also directly related to grounding line migration. We find that tidal forcing leads to an asymmetry of the flux, which increases the mean flux compared to the steady state with no forcing. In the purely viscous case we observe a difference of 0.77%. Smaller elastic parameters lead to further increase of the flux. At a value of 1×10^9 Pa for Young's modulus the difference amounts to 3.57%. This means by not accounting for the effect of tides and viscoelasticity, we neglect a significant effect for the mass balance of ice sheets. However, the obtained values are only valid for our specific geometry and setup and further research has to be done to determine the importance for real geometries.

When we force the model with a tidal period of 30 d we observe a difference of only 0.01%. This reflects that the response is rather viscous than elastic for such a long tidal period.

We show that our model is able to reproduce tidally induced grounding line migration. In the interaction of tides and flow velocity we identified two different processes that control the speed at which the ice flows. When the ice is uplifted by the tide, the area in contact with the bedrock gets smaller and therefore basal drag is reduced leading to higher velocity. At the same time the high tide causes increased normal stress at the ice – water boundary, which reduces the velocity. The superposition of these two effects controls the flow speed.

We observe velocity overshooting whenever the grounding line retreats one element. This overshoot is clearly attributed to the Maxwell material's response to a sudden change. Interestingly the overshoot in the case of an advance is much smaller. The cause for this phenomenon has not yet been revealed and further studies are necessary.

Over the observed period the grounding line does not migrate symmetrically around its steady state, but shows a constant retreat. This occurs for the Maxwell case as well as in the purely viscous case and implies that tides possibly lead to a different equilibrium state.

A comparison of the grounding line behaviour at two differently inclined beds reveals that a more shallow bed does not automatically lead to a migration over a larger area. The reason for that is not yet understood and shows the importance of conducting further simulations.

The grounding line position over time does not depend on the elastic parameter and is the same for the purely viscous case. We explain this by the relatively slow change of forcing. Studies with more rapidly changing tides have to be conducted, but with a smaller amplitude. This in turn, makes a much higher resolution necessary. It is difficult

to investigate the effect of the grid size, since different grid sizes lead to different equilibrium positions and therefore, new steady states have to be computed and the comparison among those yields new problems. Nevertheless this should be the next steps in future research on this topic.

We have shown, that the selection of an appropriate material model and the inclusion of tides have significant influence on the results of ice models and should therefore be considered at large scale modelling. This will give rise to new problems, because the model calculations are expansive in time. In large scale modelling we are often interested in timescales of a couple of hundreds, or even thousands, of years, which is not feasible with our model at the moment. It is necessary to optimize the numerical implementation a lot and we still have the problem that very small time steps are necessary to correctly incorporate the viscoelastic behaviour. Additionally, the forcing limits the maximum time step, since we are not able to resolve changes smaller than the time step.

Finally we have to take into account that in reality we deal with complex geometries and not just uniformly inclined beds. The next step to a future three dimensional model of a real geometry could be to add small scale undulations at the ice base and study the effect. Retrograde beds in combination with ice rises are also interesting because this could be applied to the situation of West Antarctica.

The grounding line is the defining boundary between ice and ocean and its importance can hardly be overstated. Obtaining further insight on the processes at the grounding line is crucial for the understanding of the whole system.

Bibliography

- Altenbach, J. and H. Altenbach (1994). *Einführung in die Kontinuums-Mechanik*. Teubner Verlag. ISBN: 3519030969.
- Christensen, Richard M. (1982). *Theory of Viscoelasticity*. 2nd ed. New York: Academic Press. ISBN: 048642880.
- COMSOL (2012a). *COMSOL Multiphysics Reference Manual*. v. 4.3. Comsol.
- COMSOL (2012b). *COMSOL Multiphysics User's Guide*. v. 4.3. Comsol.
- Durand, Gael et al. (2009). "Full Stokes modeling of marine ice sheets: influence of the grid size." In: *Annals of Glaciology* 50.52, pp. 109–114. DOI: doi : 10 . 3189 / 172756409789624283.
- Findley, W.N., J.S. Lai, and K. Onaran (1976). *Creep and Relaxation of Nonlinear Viscoelastic Materials: With an Introduction to Linear Viscoelasticity*. Dover Civil and Mechanical Engineering Series. Dover. ISBN: 9780486660165.
- Franca, Leopoldo P and Sérgio L Frey (1992). "Stabilized finite element methods: II. The incompressible Navier-Stokes equations." In: *Computer Methods in Applied Mechanics and Engineering* 99.2, pp. 209–233.
- Gerya, Taras (2009). *Introduction to numerical geodynamic modelling*. Cambridge University Press.
- Glen, J. W. (1955). "The Creep of Polycrystalline Ice." In: *Proceedings of the Royal Society of London. Series A. Mathematical and Physical Sciences* 228.1175, pp. 519–538. DOI: 10 . 1098/rspa. 1955 . 0066.
- Greve, Ralf and Heinz Blatter (2009). *Dynamics of Ice Sheets and Glaciers*. Springer.
- Gudmundsson, G. H. (2011). "Ice-stream response to ocean tides and the form of the basal sliding law." In: *The Cryosphere* 5.1, pp. 259–270. DOI: 10 . 5194/tc-5-259-2011.
- Helm, V., A. Humbert, and H. Miller (2014). "Elevation and elevation change of Greenland and Antarctica derived from CryoSat-2." In: *The Cryosphere Discussions* 8.2, pp. 1673–1721. DOI: 10 . 5194/tcd-8-1673-2014.
- Hindmarsh, Alan C. et al. (2005). "SUNDIALS: Suite of Nonlinear and Differential/Algebraic Equation Solvers." In: *ACM Trans. Math. Softw.* 31.3, pp. 363–396. ISSN: 0098-3500. DOI: 10 . 1145/1089014 . 1089020.

- Jellinek, H. H. G. and R. Brill (1956). "Viscoelastic Properties of Ice." In: *Journal of Applied Physics* 27, pp. 1198–1209. DOI: 10.1063/1.1722231.
- Joughin, Ian, Benjamin E. Smith, and Brooke Medley (2014). "Marine Ice Sheet Collapse Potentially Under Way for the Thwaites Glacier Basin, West Antarctica." In: *Science* 344.6185, pp. 735–738. DOI: 10.1126/science.1249055.
- Lohse, Johannes (2012). "Tidally induced ice dynamics at the calving front of Ekstroemisen, Antarctica, in the context of flow and fracture mechanics." Master Thesis. University of Hamburg.
- Malvern, Lawrence E. (1969). *Introduction to the Mechanics of a Continuous Medium*. 1st ed. Prentice Hall. ISBN: 0 13 487603 2.
- Moll, Albert (2007). "Radarinterferometrische Untersuchungen mit ERS-1/2 auf der Antarktischen Halbinsel." Doctoral dissertation. Rheinische Friedrich-Wilhelms Universität Bonn.
- Nye, J. F. (1957). "The Distribution of Stress and Velocity in Glaciers and Ice-Sheets." In: *Proceedings of the Royal Society of London. Series A. Mathematical and Physical Sciences* 239.1216, pp. 113–133. DOI: 10.1098/rspa.1957.0026.
- Paterson, W. S. B. (1994). *The Physics of glaciers*. 3rd ed. Oxford, England: Pergamon Press. ISBN: 0-08037945 1.
- Pattyn, F. et al. (2012). "Results of the Marine Ice Sheet Model Intercomparison Project, MISMIIP." In: *The Cryosphere* 6.3, pp. 573–588. DOI: 10.5194/tc-6-573-2012.
- Reddy, J.N. and D.K. Gartling (2010). *The Finite Element Method in Heat Transfer and Fluid Dynamics, Third Edition*. Computational Mechanics and Applied Analysis. Taylor & Francis. ISBN: 9781420085983.
- Reeh, Niels et al. (2003). "Tidal bending of glaciers: a linear viscoelastic approach." In: *Annals of Glaciology* 37.1, pp. 83–89. DOI: 10.3189/172756403781815663.
- Rignot, E. et al. (2014). "Widespread, rapid grounding line retreat of Pine Island, Thwaites, Smith, and Kohler glaciers, West Antarctica, from 1992 to 2011." In: *Geophysical Research Letters* 41.10, pp. 3502–3509. ISSN: 1944-8007. DOI: 10.1002/2014GL060140.
- Vaughan, D.G. et al. (2013). *Observations: Cryosphere*. Tech. rep. Cambridge University Press, Cambridge: Climate Change 2013: The Physical Science Basis. Contribution of Working Group I to the Fifth Assessment Report of the Intergovernmental Panel on Climate Change.

List of Figures

1.1	Principle of the grounding line – ocean tide interaction	2
1.2	Quadruple InSAR image of the Wilkins shelf ice.	2
2.1	Shear experiment for a block of polycrystalline ice	7
2.2	Hookean spring and Newtonian dashpot	8
2.3	Comparison of the Burger model to the Maxwell model	9
2.4	Geometry of the ice sheet - ice shelf system	11
3.1	Screenshot of the COMSOL GUI	16
3.2	Geometry domains	18
3.3	Mesh of the flow model	19
3.4	Replacement of the stress equations	21
3.5	Default Laminar Flow compared to the modified version including Maxwell's model.	21
3.6	Solver sequence	26
3.7	Geometry and boundary conditions of ISMIP-HOM Experiment D	28
3.8	Comparison of the Maxwell model to the mmr1 model	29
3.9	Setup for the stress build-up in a viscoelastic maxwell body.	30
3.10	Comparison of solutions for viscoelastic stress build-up	31
4.1	Horizontal velocities at different distances to the grounding line Exp. 1	35
4.2	Horizontal surface velocity at a distance of 87 km upstream of the grounding line	36
4.3	Maximum of the surface velocity over the distance to the grounding line	37
4.4	Flux across the grounding line for different elasticity parameters	38
4.5	Flux across the grounding line for a tidal period of $T = 30$ d	39
4.6	Horizontal surface velocity for $m = 1/3$	40
4.7	Horizontal surface velocity for $m = 1$	41
4.8	Results for Exp. 2 at a distance of 6 km upstream	43
4.9	Results for Exp. 2 for a shallower geometry	44

List of Tables

3.1	Parameters in the viscoelastic ice flow model	17
3.2	Flow variables	20
3.3	Contact variables	23
3.4	Flow parameters for the ISMIP-HOM Experiment D	28
4.1	Tidal constituents used in the experiments	33
4.2	Values for Young's modulus used in Exp. 1 and their respective solution times.	34
4.3	Comparison of the temporal mean flux \bar{q} over the grounding line for different elastic parameters	46

Acknowledgments

Zur Entstehung dieser Masterarbeit haben viele Menschen beigetragen. Ich möchte mich dafür bei allen bedanken. Ich danke speziell

- Angelika Humbert, für die Betreuung und Idee dieser Arbeit und dafür, immer wieder Begeisterung und Motivation für das Thema zu wecken.
- Matthias Hort, der sich bereit erklärt hat, das Zweitgutachten für meine Arbeit zu erstellen.
- Martin Rückamp, ohne den ich diese Arbeit nicht hätte schreiben können. Ich danke für die großartige und geduldige Hilfe mit Comsol und die gute Stimmung in der 'letzten Bastion' der Glaziologie in Hamburg.
- Ralf Müller und seiner Arbeitsgruppe an der Technischen Universität Kaiserslautern. Diese Kooperation hat die Arbeit erst ermöglicht.
- Julia Christmann und Carolin Plate, die mir Materialmodelle erklärt und mich supernett für zwei Wochen in Kaiserslautern aufgenommen haben.